

1 **Spatiotemporal mapping of invasive yellow sweetclover blooms using Sentinel-2 and high-
2 resolution drone imagery**

3
4 Sakshi Saraf^{1,*}, Ranjeet John^{1,2}, Venkatesh Kolluru², Khushboo Jain², Geoffrey Henebry^{3,4}, Jiquan
5 Chen^{3,4}, Raffaele Laforteza⁵

6
7
8 *Corresponding author: Sakshi Saraf; Email: Sakshi.Saraf@coyotes.usd.edu; Orcid: 0000-0002-6785-
9 8381

10
11 1. Department of Biology, University of South Dakota, Vermillion, SD 57069, USA
12 2. Department of Sustainability and Environment, University of South Dakota, Vermillion, SD 57069,
13 USA
14 3. Department of Geography, Environment, and Spatial Sciences, Michigan State University, East
15 Lansing, MI 48824, USA
16 4. Center for Global Change and Earth Observations, Michigan State University, East Lansing, MI 48823,
17 USA
18 5. Department of Soil, Plant and Food Sciences (DISSPA), University of Bari “Aldo Moro”, Via
19 Amendola 165/A, 70126, Bari, Italy
20

21 **Abstract**

22 Yellow sweetclover (*Melilotus officinalis* (L.) Lam.; MEOF) is an invasive forb pervasive across
23 the Northern Great Plains [in the United States](#), often linked to traits such as wide adaptability,
24 strong stress tolerance, and high productivity. Despite MEOF's prevalent ecological-economic
25 impacts and importance, knowledge of its spatial distribution and temporal evolution is
26 extremely limited. Here, we aim to develop a spatial database of annual MEOF abundance
27 (2016-2023) across western South Dakota (SD) at 10 m spatial resolution by applying a
28 generalized prediction model on Sentinel-2 imagery. We collected *in situ* quadrat-based total
29 vegetation cover with MEOF percent cover estimates across western SD from 2021 through
30 2023 and synthesized with other available percent cover estimates (2016-2022) of several
31 federal, state, and non-governmental sources. We conducted drone overflights at 14 sites across
32 Butte County, SD in 2023 to develop very high spatial resolution (4-6 cm) and accurate MEOF
33 cover maps by applying a random forest (RF) classification model. The field-measured and
34 uncrewed aerial system (UAS) derived MEOF percent cover estimates were used to train, test,
35 and validate a RF regression model. The predicted MEOF percent cover dataset was validated
36 with UAS-derived percent cover in 2023 across four sites (out of 14 sites). We found that the
37 variation in the Normalized Difference Moisture Index and Distance to roads were among the top
38 predicting variables in predicting MEOF abundance. Our predictive model yielded greater
39 accuracies with an R² of 0.76, RMSE of 15.11%, MAE of 10.95%, and MAPE of 1.06%. We
40 [further](#) validated our 2023 predicted maps using the 3-m resolution PlanetScope imagery for
41 regions where field samples could not be collected in 2023. The database of MEOF abundance
42 showed consecutive years of average or above-average precipitation yielded a higher MEOF
43 abundance across the study region. The database could assist local land managers and
44 government officials pinpoint locations requiring timely land management to control the rapid
45 spread of MEOF in the Northern Great Plains. The developed invasive MEOF percent cover
46 datasets are freely available at the figshare repository
47 (<https://doi.org/10.6084/m9.figshare.29270759.v1>).

48

49 Keywords: Invasive, UAV, random forest, Planet imagery, [Yellow sweetclover](#)

50 **1. Introduction**

51 **+**

52 Invasive plant species pose severe threat on ecosystem structure and services, functioning, and
53 structures (Rai and Singh, 2020). In particular, the Northern Great Plains (NGP) grasslands in the
54 United States are being threatened by long-established and newly arrived invasive plant species
55 and loss of diversity (Hendrickson et al., 2019). These invasive species compete against native
56 species, diminishing ecological goods and services and degrading vulnerable grassland
57 ecosystems (Gaskin et al., 2021). Furthermore, the ecosystem responses of grasslands in general
58 including NGP are becoming increasingly variable in space and time due to the myriad
59 influences from climate change (Bernath-Plaisted et al., 2023; Cleland et al., 2013; Zhang et al.,
60 2022). These conditions accelerate and contribute to the difficult to predict dynamics of invasive
61 plant species that often are spread unintentionally (Spiess et al., 2020). The NGP
62 comprises public, tribal, and private lands, resulting in a patchwork of management goals and
63 invasive plant control strategies (Langholz, 2010). Ecological studies that operate within
64 restricted spatial boundaries or plot-based datasets are advantageous in providing comprehensive
65 insights into local invasion scenarios (Martins et al., 2016). However, previous studies often lack
66 important spatiotemporal data on invasion dynamics, such as changes in species cover, spread
67 rates, and environmental drivers, making it difficult to fully understand invasion processes that
68 unfold continuously across space and time previous studies often miss important data, making it
69 hard to understand invasion processes that happen continuously over space and time (Larson et
70 al., 2020). Developing timely updates of the spatial and temporal spread of invasive plant species
71 therefore have been increasingly suggested to effectively and efficiently address the
72 challenges posed by invasive species in changing habitats is an urgent need (Van Rees et al.,
73 2022).

74 **Formatted:** Indent: Left: 0.25", No bullets or
75 numbering

76 In general, understanding the spatio-temporal patterns of a biennial plant species that are either
77 ephemeral in nature or bloom in specific years is challenging due to their phenological cycle.

78 One such case we have for an invasive plant named yellow sweetclover (*Melilotus officinalis* (L.)
79 Lam., MEOF) across the Northern Great Plains. There has been little to no literature on mapping
80 blooms of such plant species till the previous decade. Yellow sweetclover (*Melilotus officinalis*
81 (L.) Lam., MEOF), a common invasive legume in the NGP, exemplifies this biennial phenology.
82 There has been little to no literature on mapping blooms of such plant species until the 2010s. In
83 recent years, MEOF has attracted attention from land managers in South Dakota (SD) as it is
84 becoming a prominent invasive species in the NGP region. We refer to years with MEOF super
85 blooms (Preston et al., 2023) in the Dakota region as "sweetclover years". MEOF is a nitrogen-
86 fixing, biennial legume forb native to Eurasia (Luo et al., 2016). It has noticeable pea-like,
87 strongly scented yellow flowers arranged in a narrow raceme, which can grow more than 4 cm
88 long (Varner, 2022). The ability of MEOF to establish and grow in a wide range of temperature,
89 precipitation, and soil conditions has naturalized its presence in the NGP region (Kan et al.,
90 2023). It is often one of the first plants to appear in disturbed or open sites, including pastures,
91 agricultural fields, roadsides, rangelands, and open slopes in badlands, prairies, or floodplains
92 (Wolf et al., 2003).

93 **Formatted:** Space After: 0 pt

94 **Formatted:** Font: 12 pt, Font color: Auto, Ligatures:
95 None

96 **Formatted:** Font: 12 pt, Font color: Auto

97 **Formatted:** Font color: Auto

98 **Formatted:** Font: 12 pt, Font color: Auto

99 **Formatted:** Font: 12 pt

100 **Formatted:** Space After: 0 pt

93 Invasive forbs such as MEOF develop yellow inflorescences with yellow flowers that are
94 prominent during flowering time and can be detected using 10 m resolution Sentinel-2 derived
95 reflectance and quantitative indices, provided the plants meet the optimal size or developmental
96 stage for detection (Saraf et al., 2023). Previous studies have shown that multi-temporal analysis
97 using remote sensing data can be a powerful tool for addressing challenges in monitoring
98 invasive species dynamics (Bradley, 2014; Mouta et al., 2023). For exampleS, Sentinel-2
99 imagery with 10 m spatial resolution has sufficed for mapping a range of invasive plant species
100 (Kattenborn et al., 2019). In addition, the high temporal resolution of the Sentinel-2 can help
101 capture phenological information characteristics and identify species with pronounced flowering
102 periods. However, there have been relatively very few efforts to map MEOF in the NGP due, in
103 part, to its unreliable annual aboveground establishment resulting in low to moderate abundance
104 during drier years complicating attempts to map its distribution. Moreover, its yellow flowers can
105 be easily mistaken for other in remote sensing imagery for other yellow-flowered forbs such as
106 yellow salsify, black eyed susan, western wallflower, annual sunflower or leafy spurge. MEOF
107 tends to grow in dense patches and invade vast areas with the capability of growing up to 2 m tall
108 when ample moisture is available during its growth period. In the recent wet year of 2019,
109 MEOF thrived across the NGP, resulting in minimal spatial overlaps with other yellow flowered
110 plants and enabling researchers to map its spatial distribution. Specific years with an enhanced
111 bloom of MEOF, such as 2019 and 2023, were easily distinguished in image time series due to
112 their extensive spread, tall canopy, and prolific yellow flowers during summer (Preston et al.,
113 2023). Such climate conditions create an opportunity to collect more ground samples to increase
114 accurate mapping of MEOF distribution.

← Formatted: Space After: 0 pt

115
116 In traditional remote sensing, *in situ* reference data are required to detect and validate complex
117 patterns and ecologically relevant processes (Mayr et al., 2019). The reference data collection is
118 usually labor-intensive, time-consuming, and logistically difficult across large spatial areas.
119 Uncrewed Aerial Systems (UAS), combined with high-resolution multispectral or hyperspectral
120 cameras, offer an interesting promising, user-friendly, and low-cost alternative data source to *in*
121 *situ* data collection (Horstrand et al., 2019; Li and Tsai, 2017; Rakotoarivony et al., 2023).
122 Despite the limited spatial extent of each swatch, UAS still enables the acquisition of spatially
123 continuous information on species cover with ultra-high spatial resolution (e.g., Gground
124 Ssampling Distance of <10 cm) and temporal flexibility (Turner and Wallace, 2013). Numerous
125 studies have demonstrated the potentials of UAS data as an alternative source to supplement or
126 even replace the traditional sampling methods of detecting species presence in the field (Alvarez-
127 Taboada et al., 2017; Baena et al., 2017; Kattenborn et al., 2019). UAS data can be used to train
128 models that employ fine-to-medium spatial resolution data, such as Sentinel-2 imagery, to map
129 invasives at regional scales (Preston et al., 2023), despite a small survey extent (Colomina and
130 Molina, 2014).

← Formatted: Space After: 0 pt

131
132 Previously, we lacked sufficient statistical power and comprehensive spatial coverage due to
133 small sample size to conduct regional scale mapping for the 2019 MEOF blooms (Saraf et al.,
134 2023). Preston et al., (2023) used an ensemble of MaxEnt models to map MEOF fractional cover
135 for 2019 using UAS data from 16 sites spread across three counties in SD and Montana using

136 satellite imagery trained from regional UAS imageries. Our team also examined the contribution
137 of various biophysical factors to MEOF and tested different machine learning algorithms to
138 determine the best algorithmapproach to map the MEOF for 2019 (Saraf et al., 2023). We found
139 that the random forest (RF) modelalgorithm (Breiman et al., 1984) outperformed other machine
140 learning algorithms in mapping the distribution of invasive MEOF cover. However, our results
141 also indicated a significant underestimation of the percent cover due to the limited sample size.
142 We, therefore, aimed to increase the sampling size by collecting quadrat-based percent cover and
143 UAS imagery over MEOF blooms and synthesizing estimates from various state and federal
144 sources to overcome uncertainties and the limitation of underestimation.

145
146 We endeavored attempted to optimize the utilization of UAS and Sentinel-2 data to create a
147 reference percent cover dataset, which was then used as a training and validation inputs for a RF
148 modeling framework. This approach helped develop an annual time-series percent cover
149 database for the invasive MEOF. Developing a generalized model enables efficient mapping of
150 irruptive invasive plant species that blooms episodically, often found in clustered patches with
151 poor representation in the field data. Developing a generalized model that can be applied across
152 space and time allows for efficient mapping of irruptive invasive plant species, which often
153 bloom episodically and occur in clustered patches. Such distributions are often underrepresented
154 in conventional field survey datasets, including our ground reference data, because random
155 sampling rarely captures them adequately. Effective Management of plant invasives such as
156 MEOF will require spatially continuous, multitemporal maps of species occurrence and cover as
157 its first step. Building such a database for invasive MEOF can help to comprehend the spatial
158 and temporal dynamics of its invasion patterns (Müllerová et al., 2017). Therefore, our
159 objectives are threefold: (1) to develop a generalized prediction model using field-collected and
160 UAS-derived percent cover samples along with Sentinel 2 imagery to map the extentfractional
161 cover of invasive MEOF using Sentinel 2 imagery across western SD; (2) to compare and
162 validate our model-derived percent cover estimates against the drone-derived estimates; and (3)
163 to further validate the predicted yellow sweetclover maps using PlanetScope imagery, which
164 provides higher temporal resolution and independent data for cross-sensor validation, and to
165 assess MEOF cover in regions lacking UAS coverage to validate the predicted yellow
166 sweetclover maps independently using PlanetScope imagery. We ask two research questions.
167 First, what are the spatiotemporal distributions of invasive MEOF across western SD? Second,
168 are the spatiotemporal distributions of MEOF explained by precipitation in bloom years? For
169 land managers, it is crucial to both understand the current distribution of MEOF in recent years
170 and appreciate its invasion dynamics, to curb further spread of MEOF into previously unaffected
171 areas. The developed invasive species cover database would therefore, help to design mitigation
172 strategies effectively and promote the proactive conservation of grassland ecosystems.

173
174 **2. Methods**

175 **2.**

176 **2.1 Study Area**

177

Formatted: Space After: 0 pt

Formatted: Font: Ligatures: None

Formatted: Indent: Left: 0.25", No bullets or
numbering

178 Western SD is located within the Upper Missouri River Basin and is a part of the NGP,
179 characterized by the Black Hills along with prairie at the southwestern corner, along with high
180 buttes, canyons, and wide expanses of nearly level tablelands (Figure 1). This region experiences
181 a semi-arid climate with high interannual variability in precipitation, averaging around 300-400
182 mm (Agnew et al., 1986). About three-fourths of the ~~rainfall~~ ~~precipitation~~ occurs during summer,
183 and snowfall ranges from 650 mm to 5000 mm throughout western SD (Paul et al., 2016).
184 Despite the substantial conversions of rangeland to cultivated lands in the U.S. Midwest, most of
185 the central and western SD landscapes are still dominated by rangelands. The landscape of
186 western SD is a mosaic of mixed-grass prairie interspersed with ~~shrub~~ ~~cultivated lands~~. The
187 mixed grass prairie shifts into shortgrass and sagebrush grassland in the extreme western portion
188 of the state. The dominant grasses include western wheatgrass (*Pascopyrum smithii* (Rydb.) Å.
189 Löve), needle and thread (*Hesperostipa comata* (Trin. & Rupr.) Barkworth), little bluestem
190 (*Schizachyrium scoparium* (Michx.) Nash), prairie sandreed (*Calamovilfa longifolia* (Hook.)
191 Scribn), green needlegrass (*Nassella viridula* (Trin.) Barkworth), blue grama (*Bouteloua gracilis*
192 (Willd. ex Kunth.) Lag. ex Griffiths) and threadleaf sedge (*Carex filifolia* Nutt.). Dryland sedges
193 (*Carex spp.* L.), prairie threeawn (*Aristida oligantha* Michx.), and fringed sagewort (*Artemisia*
194 *frigida* Willd.) increase with disturbance (Owensby and Launchbaugh, 1977; Reinhart et al.,
195 2019; Sanderson et al., 2015). Several perennial forbs such as western wallflower (*Erysimum*
196 *asperum* (Nutt.) DC.), Canada thistle (*Cirsium arvense* (L.) Scop.), leafy spurge (*Euphorbia*
197 *esula* L.), purple prairie clover (*Dalea purpurea* Vent. var. *purpurea*) and shrubs such as big
198 sagebrush (*Artemisia tridentata* Nutt.), broom snakeweed (*Gutierrezia sorothrae* Pursh) and
199 leadplant (*Amorpha canescens* Pursh) are prevalent. The most common invasive grasses include
200 Kentucky bluegrass (*Poa pratensis* L.), smooth brome (*Bromus inermis* Leyss.), cheatgrass
201 (*Bromus tectorum* L.), and curlycup gumweed (*Grindelia squarrosa* (Pursh) Dunal). Yellow
202 salsify (*Tragopogon dubius* Scop.) and yellow sweetclover (*Melilotus officinalis* (L.) Lam.) are
203 common invasive annual-biennial forbs in this region (Johnson and Larson, 1999).

204 Formatted: Space After: 0 pt

205 2.2 UAS Survey

206 Ultra-high spatial resolution UAS imagery were acquired ~~at~~ ~~for~~ 14 sites during a field campaign
207 from July 9 to July 15, 2023. ~~The flight locations were randomly selected across Butte County in~~
208 ~~western SD based on the availability of the larger patches of MEOF. The flight locations were~~
209 ~~randomly selected across Butte County in western South Dakota to capture large, continuous~~
210 ~~patches of MEOF, ensuring that the imagery encompassed the full range of percent cover within~~
211 ~~each site, including areas without MEOF.~~ -We collected multispectral (Visible, RedEdge, and
212 Near InfraRed) imagery using a MicaSense RedEdge-MX (MicaSense, 2015) camera deployed
213 on a DJI Matrice 200 UAS platform. The radiometric calibration of the sensor was implemented
214 by converting the digital values of the orthomosaic to the values of surface spectral reflectance
215 by Micasense calibration panel. The area covered for each flight ranged between 1 ha and 10 ha,
216 depending on the patch size of the MEOF invasion (Table S7). The imagery was captured with at
217 least 80% forward and 75% side overlap (Table 1). We flew the flight at an average altitude of
218 30-60 m above ground, ensuring a spatial resolution of at least 3 cm. We used the recorded
219 inertial measuring unit (IMU) and Global Navigation Satellite System (GNSS) module of the
220 UAS along with Real-Time Kinematic (RTK) positioning (~1 cm accuracy) to guide the drone
221

222 Formatted: Font: Not Bold

222 by placing four Ground Control Points (GCPs) at each site to ensure the geometric accuracy of
223 the images taken by the drone matched the Sentinel-2 imagery. Several studies have
224 demonstrated that using GCPs can lead to higher accuracies in the processed orthoimages than
225 direct georeferencing (Jurjević et al., 2020; Padró et al., 2019). Moreover, GCPs help advance
226 the upscaling of UAS to Sentinel-2 imagery with the best alignment and minimum shift (Gränzig
227 et al., 2021). Therefore, we processed the UAS images in Pix4D mapper (Pix4D S.A., 2022), and
228 georeferenced the orthomosaics using the GPS coordinates of plot center and corner targets
229 collected with Trimble Catalyst DA2 GNSS receiver kit (Trimble Inc. (n.d.), 2025) with a
230 precision level of 1 cm accuracy. Out of the 14 sampling sites, ten sites were selected for training
231 a random forest (RF) model; whereas, the other four were reserved for model validation. All 14
232 sites captured the observed range of MEOF percent cover, but they differed in total area covered
233 by MEOF presence and the number of samples derived from each site. To ensure a balanced
234 split, the 10 smaller sites were randomly selected for training the RF model, while the remaining
235 four larger sites were reserved for validation. This approach ensured that both the training and
236 validation sets contained approximately equal numbers of samples, providing an unbiased
237 assessment of model performance.

Formatted: Font: Not Bold

Formatted: Font: Not Bold

241 2.3 Field measurements and sample collection

242
243 We used a total of 22,972 MEOF percent cover samples collected across western South Dakota
244 rangelands and surrounding regions during 2016–2023 (Table S1). This included 5,283 samples
245 derived from UAS imagery collected during the peak blooming months (June–August) in 2023
246 (details in Sections 2.2 and 2.4) across western South Dakota rangelands. In addition, 17,689
247 MEOF cover samples were retrieved and synthesized from multiple federal, state, and non-
248 governmental sources for 2016–2022 across four states: South Dakota, North Dakota, Montana,
249 and Wyoming (Figure 1a; Table S1). We conducted multiple field surveys during peak blooming
250 months (June–July–August) across western SD rangelands from 2021 to 2023 (Table S1). We
251 implemented a conventional plot based quadrat method to estimate percent cover by averaging
252 the grids occupied with MEOF. A minimum of three samples were collected within a 30 m × 30
253 m plot using 0.5 m × 0.5 m quadrats (John et al., 2018). For 2023, the GPS locations of the field-
254 collected quadrat samples were utilized as the ground control points for enhancing the processing
255 of drone imagery to derive percent cover samples. We retrieved 17,689 MEOF cover samples
256 from several federal, state, and non-governmental sources for 2016–2022 across four states:
257 South Dakota, North Dakota, Montana, and Wyoming (Figure 1a), as described in Table S1.
258 Although the historical samples were obtained using different field protocols, they were
259 integrated with our field-collected data to increase spatial and temporal coverage. These sources
260 included RCMAP data from the USGS Center for Earth Resources Observation & Science,
261 USGS Northern Rocky Mountain Science Center (Montana), the Bureau of Land Management
262 (BLM) database, the Northern Great Plains Inventory & Monitoring Network, the National
263 Ecological Observatory Network (NEON), and the Montana Natural Heritage Program. The
264 source, year-wise distribution, and frequency of the samples are summarized in Tables S2 and
265 S3. The samples' source, year-wise distribution, and frequency distribution are given in Tables S2

Formatted: Font color: Text 1, Do not check spelling or
grammar

Formatted: Font: Not Bold

Formatted: Line spacing: Multiple 1.08 li

Formatted: Font: Not Bold

Formatted: Font: (Default) Times New Roman, 12 pt,
Ligatures: None

266 and S3. At the 10 m mapping scale, this compilation provided a suitable reference for model
267 training and validation. Our field-collected surveys recorded the plant species composition,
268 including dominant species and percent cover of all species present, using the conventional plot-
269 based quadrat method. Within each 30 m × 30 m plot, a minimum of three 0.5 m × 0.5 m
270 quadrats were sampled. Percent cover for each plot was calculated as the average of the quadrat
271 measurements, with each quadrat considered representative of its portion of the plot. Within each
272 quadrat, we estimated percent cover of MEOF by averaging the grids it occupied, allowing fine-
273 resolution observations to be scaled up to the plot level while capturing spatial variability (John
274 et al., 2018). We recorded flowering and non-flowering MEOF individuals separately. The
275 separation was done to document phenological variability and population structure, which can be
276 useful for understanding interannual flowering dynamics in future analyses. However, only the
277 flowering MEOF percent cover was used for remote sensing-based mapping, as flowering
278 individuals exhibit a distinct spectral signal that can be consistently detected in aerial and
279 satellite imagery. This approach ensured that the satellite-derived cover estimates corresponded
280 specifically to the detectable, flowering component of MEOF. For 2023, the GPS locations of the
281 field-collected quadrat samples were utilized as the ground control points for enhancing the
282 processing of drone imagery to derive percent cover samples.

Formatted: Font color: Text 1

283 ▲ 2.4 UAS derived yellow sweetclover cover
284
285

Formatted: Font: English (United States)

286 MEOF is prominently visible in orthomosaics using a combination of green, green, and blue
287 bands. This prominence occurs because yellow flowers of MEOF increase reflectance of green
288 while slightly decreasing reflectance of blue color (Sulik and Long, 2016). We first visually
289 delineated several polygons of MEOF on the georeferenced orthomosaics using these band
290 combinations. We then used 3000 absence and 3000 presence samples derived from these
291 polygons to train a machine learning classification model and classify MEOF presence pixels
292 from other land cover pixels. We used five spectral bands (Blue, Green, Red, RedEdge, and NIR)
293 and the Normalized Difference Yellowness Index (NDYI) to classify the yellow-flowered
294 blooms in the imagery. The equation for NDYI is provided in Table S4. We implemented an RF
295 classification model on randomly split 80:20 ratio samples to segregate MEOF pixels from other
296 pixels. We tuned the RF hyperparameters (mtry = 4, ntrees = 1500) to optimize model predictive
297 performance, specifically by minimizing the Root Mean Square Error (RMSE) using 10-fold, 5-
298 repeat cross-validation. We assessed model efficiency both visually, using green–green–blue
299 false color composites, and quantitatively, by calculating Overall Accuracy and the Kappa
300 coefficient. We implemented hyperparameter tuning (mtry = 4 and ntrees = 1500) and 10-fold 5-
301 repeat classification to tune the model. We tested model efficiency through visual interpretation
302 using green–green–blue false color composites along with model metrics such as Overall
303 Accuracy and Kappa coefficient (Landis and Koch, 1977). We converted the continuous RF
304 predictions to binary presence/absence using a threshold of 0.5, assigning pixels with predicted
305 probability > 0.5 as MEOF presence (assigned as 1) and pixels < 0.5 as absence (assigned as 0)
306 (Josso et al., 2023; Steen et al., 2021). The binary classified MEOF present pixels were assigned
307 with the value of 1 for present pixels and 0 for MEOF absence. We calculated the area-based
308 weighted average of MEOF classified pixels from the total number of pixels within a 10m pixel
309 to derive MEOF percent cover at 10 m resolution. The percent cover of MEOF within each 10 m

310 resolution pixel was calculated as the proportion of classified MEOF pixels within that 10 m
311 area.

312
313 We collected and averaged minimum of three field samples per 30 m × 30 m plot at each drone
314 site in 2023. Overall, we had 30 observed percent cover samples collected across 14 drone sites.
315 We employed a jackknife resampling procedure using leave-one-out cross-validation to calibrate
316 RF classification-derived percent cover estimates of MEOF against field-observed percent cover
317 values. For each iteration, one observation was excluded from the dataset, and a linear regression
318 model was fitted using the remaining field samples. The excluded field observation's field cover
319 was then predicted using the fitted model, based solely on its derived cover value. This process
320 was repeated for all observations, resulting in a set of cross-validated predictions for the entire
321 dataset. Calibration accuracy was assessed by comparing predicted and observed values using
322 root mean square error (RMSE) and the correlation coefficient of determination (R^2). We used
323 linear regression to calibrate RF-derived percent cover estimates because it provides a simple
324 and transparent way to correct systematic biases. To ensure unbiased predictions and minimize
325 overfitting, we applied a leave-one-out jackknife procedure, where each observation was
326 predicted independently of the data used to fit the model. We calibrated the derived percent cover
327 values using the calibrated samples. This jackknifing approach provides an unbiased estimate of
328 model performance and accounts for overfitting, ensuring that each prediction is made
329 independently of the observation being predicted (Wolter, 2007).

330
331 We combined the MEOF samples collected in the field from 2016-2022 with UAS-derived 5283
332 samples from 2023, resulting in a total of 22,972 samples. We removed the duplicate samples
333 from different sources falling within the same pixel location for the same year. After removing
334 the duplicates, we had 20,275 sample points. We calculated the Global Moran's I to estimate the
335 spatial autocorrelation between the samples within each year. Due to high positive spatial
336 autocorrelation for samples in 2019, we removed samples within a 50-m distance for 2019 and
337 used the remaining 11,235 samples for the random forest regression model. We then combined
338 field and UAS-derived samples from 2016-2023, resulting in a total of 22,972 MEOF percent
339 cover samples for the regional-scale regression analysis described in Section 2.6 and shown in
340 Figure 2.

341
342
343 2.5 Satellite-derived predictor variables

344
345 We obtained 64 predictor variables with spatial resolutions ranging between 10 m and 1 km. We
346 derived maximum value composites of various indices and tasseled caps for the peak summer
347 months with a maximum of 10% cloud cover to enhance the spectral information of the Sentinel
348 2A imagery (Table S4) (Gascon et al., 2017). We also derived the coefficient of variation
349 (standard deviation/mean) composites to represent the variability of the indices or the tasseled
350 cap components across the summer months. For variables affected by high cloud cover or limited
351 image availability in the seasonal composites, we used the standard deviation as an alternative to
352 the coefficient of variation.

353
354 For climate predictors, we utilized the Daymet- monthly and annual dataset (Version 4R1)
355 available at 1 km spatial resolution (Thornton et al., 2022). From the monthly data, we calculated

356 mean annual precipitation (MAP) as the sum of monthly precipitation values and mean annual
357 temperature (MAT) as the average of the monthly mean temperatures for each year
358 corresponding to the MEOF cover samples. To account for potential biennial effects, we also
359 calculated biennial precipitation (MAP2) and biennial temperature (MAT2) by combining the
360 values from the sample year with those of the preceding year (e.g., total precipitation across both
361 years and average temperature across both years). We also computed seasonal composites of
362 precipitation and mean temperature for each year separately corresponding to the MEOF cover
363 samples, including spring (March–May; P_{MAM} and T_{MAM}) and summer (June–August;
364 P_{JJA} and T_{JJA}). We derived mean annual and biennial total precipitation (MAP and MAP2)
365 and temperature (MAT and MAT2) from the Daymet dataset (Version 4R1) available at 1 km
366 spatial resolution (Thornton et al., 2022). We also computed seasonal composites
367 (Mar+Apr+May and Jun+Jul+Aug) for total precipitation (P_{MAM} and P_{JJA}) and mean temperature
368 (T_{MAM} and T_{JJA}). We acquired percent snow cover at 500m resolution from the MODerate
369 resolution Imaging Spectroradiometer (MODIS) MOD10A1 V6.1 snow cover product (Riggs et
370 al., 2015). Snow depth and snow water equivalent were acquired at 1 km spatial resolution from
371 NOAA National Weather Service's SNOW Data Assimilation System (SNODAS) (Barrett, 2004).
372 We computed mean composites for all snow variables during the winter (Dec+Jan+Feb).
373

374 For soil properties, we obtained soil pH, texture (sand, silt, clay, and bulk density), volumetric
375 water content, saturated water content, and soil organic matter from the Polaris database (Chaney
376 et al., 2019) available at 30 m resolution. For terrain features such as elevation, slope, aspect, hill
377 shade, terrain wetness index, and terrain roughness index, we used the National Elevation
378 Dataset from the NASA Earthdata portal available at 10 m resolution. We used the National
379 Elevation Dataset from the NASA Earthdata portal available at 10 m resolution to derive
380 elevation, slope, aspect, hillshade, terrain wetness index, and terrain roughness index. We used a
381 land cover/use map to mask out non-rangeland areas before implementing the regression model
382 to emphasize the habitat of MEOF in the western SD rangelands. The land cover/use data and the
383 proximity to roads were derived at 30 m resolution from the 2019 National Land Cover Database
384 (NLCD 2019, Dewitz, 2021). We also derived the distance to developed/urban areas, including
385 non-primary roads as a proxy for proximity to roads. Lastly, the distance to stream product was
386 derived from the national hydrography dataset developed by the U.S. Geological
387 Survey National Geospatial Program. All the variables were acquired from the Google Earth
388 Engine (GEE) platform and processed in ArcMap 10.8.1. All variables were resampled to 10 m
389 resolution and projected in Albers Equal Area projection and WGS 84 datum. We used bilinear
390 interpolation for predictor variables to preserve data integrity during resampling. A detailed
391 summary of all the independent variables utilized in this study is provided in Table S5. The
392 method workflow for predicting the invasive yellow sweetclover percent cover for 2016–2023 is
393 illustrated in Figure 2.

394 2.6 Regional MEOF cover regression model

395 We compiled a total of 22,972 MEOF percent cover samples for the regional-scale regression
396 analysis. After removing duplicate records (samples from different sources falling within the
397 same pixel and year), 20,275 unique samples remained. Most machine learning models such as
398 RFs work on the assumption that the samples are independent and identically randomly
399 400

Formatted: Font: Not Bold

Formatted: Space After: 0 pt

401 distributed. If this assumption is violated due to spatial autocorrelation, model performance
402 metrics (like accuracy, R^2) can be overestimated (Liu et al., 2022). To deal with this issue, we
403 calculated Global Moran's I with a minimum distance of 50 m on the MEOF percent cover
404 samples to test for spatial autocorrelation between the samples within each year (Moran, 1950).
405 We implemented permutation test for the samples to generate the null distribution and assess the
406 significance of the Moran's I. A 50 m threshold is equivalent to five pixels which helps in
407 mitigating the influence of immediate neighbors, which often exhibit strong spatial
408 autocorrelation due to their proximity. By setting this distance, we aimed at reducing local
409 clustering and while ensuring a degree of spatial independence among samples, which is critical
410 for robust estimation of global spatial autocorrelation. Similar buffer distances have been used in
411 previous ecological studies to distinguish between fine-scale spatial dependence and broader
412 spatial patterns, particularly in heterogeneous landscapes where plant cover could be spatially
413 clustered at short ranges (Baumann et al., 2025). We removed the spatially-correlated samples
414 and later used 11,235 observed samples to develop a generalized percent cover regression model
415 using the Random Forest algorithm (Breiman et al., 1984). We constructed a predictor
416 variable database by extracting observed sample points from the satellite-derived predictor
417 variables (rasters) for training the RF model. We overlaid these observed samples on predictor
418 variable (rasters) to derive a predictor variable database for training an RF model. We
419 implemented a spearman correlation coefficient (r) threshold of 0.8 to remove highly correlated
420 predictor variables (Dubuis et al., 2011; Stohlgren et al., 2010; Zar, 2005). We then implemented
421 a Recursive Feature Elimination (RFE) method with 5-repeat, 10-fold cross-validation to
422 determine the top predicting variables (Breiman, 2017; Guyon et al., 2002). The observation
423 samples were split in an 80:20 ratio for training and testing sets using the bootstrap method with
424 replacement. All the variables were scaled and centered before the development of the prediction
425 model. We implemented hyperparameter tuning (*mtry* and *ntrees*) and used the mean absolute
426 error (MAE), mean absolute percentage error (MAPE), root mean square error (RMSE), and the
427 coefficient of determination (R^2) metrics to evaluate the model performance during the testing
428 phase. The MEOF percent cover was predicted using the best generalized model and the best
429 statistical metrics. We used the reference of the habitat suitability map from Saraf et al., (2023)
430 to mask out the low probability of occurrence regions and to develop final MEOF prediction
431 maps. All the analyses were performed using the 'caret' package in the RStudio environment
432 (Kuhn, 2015).

Formatted: Font: 12 pt, Font color: Text 1

433 3. Results

434 3.1 Yellow sweetclover cover from UAS imagery

435 We used 6,000 training points to train and test an RF classification model by splitting them to an
436 80:20 ratio, obtaining 4,795 training and 1,205 testing samples. The developed RF classification
437 model exhibited an overall accuracy of 98.76% and k kappa coefficient of 0.97 in distinguishing
438 flowering MEOF pixels. The confusion matrix for the classification model is provided in Table
439 S6. The RF classification accuracies can be visually validated in three exemplary representative
440 UAS sites with MEOF blooms (Figure 3). Figure 3 shows the three UAS training sites with (a)
441 UAS orthoimage with green, green, and blue band combination, (b) NDVI with darker brown
442 representing MEOF presence, (c) RF classified image showing MEOF presence, and (d) the
443 derived MEOF percent cover at 10 m pixel resolution. The estimated area covered with the
444 classified MEOF presence pixels derived from the RF classification model can be found in Table
445

447 S7. We generated 5,283 percent cover samples from UAS, which were divided into 2,736
448 samples for training sites and the remaining 2,547 samples for validating the RF regression
449 model. The samples were segregated based on ten training and four validation locations. We
450 implemented the jackknifing to calibrate the derived MEOF cover. The cross-validated
451 predictions showed good agreement with the field observed samples with the R^2 of 0.68 and
452 RMSE of 6.24%, suggesting relatively low average prediction error.

453
454 3.2 Regional-scale Random Forest predictions of MEOF cover
455

456 We used the spearman correlation test (r) on all 64 independent variables with a threshold of 0.8
457 and selected 25 predictor variables (Figure S1). We later implemented a recursive feature
458 selection on the 25 predictor variables and selected the 13 top predictor variables. The top 13
459 predictor variables included climatic variables — mean annual precipitation (MAP), coefficient
460 of variation of MAP (MAPcv), mean annual temperature (MAT), coefficient of variation of
461 MAT (MATcv), snow depth (SnowDepth), and coefficient of variation of snow depth
462 (SnowDepth_cv); topographic variables — elevation (Elevation) and slope (Slope); proximity to
463 roads (Dist_Roads); and remote sensing indices capturing moisture and vegetation properties —
464 Normalized Difference Moisture Index (NDMI), coefficient of variation of Normalized
465 Difference Water Index (NDWIcv), coefficient of variation of Land Surface Water Index
466 (LSWIcv), and coefficient of variation of Tasseled Cap Wetness (TCWcv; Table 2). (Table 2).
467 We took the threshold of 0.3 for Moran's I to reduce the positive spatial autocorrelation among
468 the samples. We used sampling with replacement to calculate the significance of the Moran's
469 I. We found that all the years except 2019 and 2023 showed very low spatial autocorrelation
470 with Moran's I of <0.2 (Table S8). We reduced the spatially autocorrelated samples for 2019 and
471 2023 by selecting samples beyond a minimum distance of 50 m. Overall, we used a total of
472 11,235 training samples to develop an RF model to predict invasive MEOF cover across western
473 SD. We used 80% of these samples (9,006 totalsamples) for training and 20% (2,229
474 samplestotal) for testing the model, with 3 mtry and 1500 ntrees as the optimized
475 hyperparameters for the regression model. We noticed that the reduction in sample size had
476 little-to-no effect on the model statistics and metrics. The developed RF model exhibited an R^2
477 of 0.76, RMSE of 15.11, MAE of 10.95, and MAPE of 1.06 %. The predicted cover maps for
478 2019 and 2023 showed a relatively higher percent cover range than those for other years (Figure
479 S2). The temporal maps showed a higher cover of MEOF in the western counties compared to
480 the eastern counties of western SD (Figure 4). We also found that the MEOF cover followed
481 moisture gradients as higher cover was evident near floodplains. We also found that the western
482 section of the study region, including Butte, Harding, Pennington, Custer, and Fall River
483 counties, were the major hotspots for MEOF cover and showed persistent higher percent cover
484 particularly in 2018, 2019 and 2023. This region tends to have a broaderwider spread of high-
485 density cover over the years. The hotspots were more evident in wet years especially along the
486 floodplains of the Missouri River tributaries, as we move along the west-to-east gradient across
487 western SD. Variable importance showed Normalized Difference Moisture Index (NDMI),
488 proximity to roads (Dist_roads), variability in Normalized Difference Water Index (NDWIcv),
489 and Elevation were the top contributing variables for predicting MEOF cover (Figure S3).

490
491 We created a MEOF percent cover map series for 2016–2023 and compared it with precipitation
492 anomaly maps to assess the potential relationship between MEOF cover and interannual climatic

Formatted: Font: (Default) Times New Roman, 12 pt,
Font color: Text 1, Ligatures: None

Formatted: Font: (Default) Times New Roman, 12 pt,
Font color: Text 1, Ligatures: None

Formatted: Font: (Default) Times New Roman, 12 pt,
Ligatures: None

Formatted: Font: (Default) Times New Roman, 12 pt
Formatted: Font: (Default) Times New Roman, 12 pt,
Font color: Text 1

Formatted: Font: (Default) Times New Roman, 12 pt,
Font color: Text 1

Formatted: Font: (Default) Times New Roman, 12 pt

Formatted: Font: (Default) Times New Roman, 12 pt,
Ligatures: None

Formatted: Font: (Default) Times New Roman, 12 pt

493 variability. These precipitation anomaly maps showed that the western SD witnessed above-
494 average precipitation in a few regions for 2018 and 2023 and most of the western SD for 2019
495 (Figure S4). The central and eastern counties in 2019 and the central and southern counties in
496 2023 showed a greater range of MEOF covers showing a consistent pattern of MEOF resurgence
497 with the return of wet conditions. Despite 2016 being a relatively normal or slightly dry year,
498 sweetclover cover remained moderate with less spatial variability, indicating less widespread
499 establishment. The widespread establishment of MEOF could be seen increasing in 2018, with a
500 high Coefficient of Variation (CV) of 0.5 and then its percent cover reached a peak in the
501 subsequent year of 2019. For the years 2020, 2021 and 2022, most regions experienced average
502 to below-average rainfall conditions. During these years, the MEOF percent cover reached up to
503 50%, with the a sharp drop in percent cover in 2021, where the maximum cover was only 43%.
504 This showed drought conditions likely limit growth and establishment. The year 2020 and 2022
505 acted as transitional years, possibly due to lagged ecological response. For dry years, the
506 majority of western SD predicted less than 50% cover.

507

508

509 Overall, we found a high percent cover range in the western counties of western SD including
510 Butte, Meade, Pennington, Custer, Fall River, Jackson, Bennet and Oglala Lakota counties.
511 Central South Dakota counties showed fluctuating trends, with moderate to high coverage in
512 some years (e.g., 2018, 2019, 2023) and relatively low coverage in other years (e.g., 2020, 2021),
513 whereas the eastern counties (i.e., Corson, Dewey, and Stanley) consistently exhibited relatively
514 low percent cover (<20%) for the majority of years. In the eastern region, MEOF appeared to be
515 more scattered and patchier with fewer patches of higher percent cover near floodplains, which
516 are situated at lower elevations and benefit from high moisture availability especially in the years
517 2018 and 2019. During the summer fieldwork of 2022, we observed MEOF predominantly in the
518 first year of its life cycle. In the following year, we observed ample coverage of MEOF blooms
519 in Butte County, SD forming patches substantial enough to be captured by the drones. This
520 temporal pattern arises from the biennial growth period of MEOF. Additionally, we predicted
521 MEOF percent cover estimates for the year 2024 using our trained model (Figure S5). This 2024
522 prediction has been validated with the Planet imagery and is yet to be validated with the field
523 samples. Validation of model performance for 2024 and subsequent years with PlanetScope
524 imagery remains a key focus for future work.

525

526

527 Year-wise evaluation of model performance revealed considerable variation in normalized
528 RMSE (nRMSE), which ranged from 0.12 in 2022 to 0.65 in 2023 (Table S9). The year-wise
529 sample distribution of observed MEOF cover could be a partial reason for these differences. In
530 2018, the observed cover exhibited the greatest variability (CV = 0.51) and reached a maximum
531 cover of 81%. However, the nRMSE remained low (0.19), indicating that the model effectively
532 captured patterns in years with a broader range of values. Conversely, 2023 exhibited the highest
533 error (nRMSE = 0.657) despite having the 100% maximum cover and the lowest variability (CV
534 = 0.25). This high error occurred despite a relatively large sample size, likely due to spatial
535 clustering and the reduced ability of the model to predict extreme cover values. Consequently,
536 the model's capacity to generalize to high-cover conditions was restricted. Similarly, 2020 had a
537 moderate maximum cover (56%) but relatively high error (nRMSE = 0.55), which may reflect
538 imbalances in sample distribution across cover classes. In contrast, the most optimal overall

Formatted: Font: 12 pt, Font color: Text 1

539 performance was achieved in 2022 (max = 57%, CV = 0.38) (nRMSE = 0.124), which implies
540 that predictive accuracy is enhanced by balanced sampling across cover ranges. These results
541 emphasize that the distribution and variability of cover values across years have a significant
542 impact on predictive performance, although increasing the sample size improves model stability.
543

544 4. Discussion

545 4.1 Significance of mapping MEOF ~~bloomssuperblooms~~

548 Our study offers a workflow for different plant species of annuals, biennials, or geophytes that
549 share dominance during the bloom events, exhibiting huge blooms in specific years with
550 differences of 4 to 10 weeks in their length and peak of the flowering period (Vidiella et al.,
551 1999). These blooms cause a sudden increase in annual net primary production, triggering
552 relevant changes in the ecosystem such as increases in soil nitrogen content due to N-fixation,
553 temporary plant composition modifications, attraction of predators, etc. (Jaksic, 2001), as well as
554 changes in the local climate: an increase in evapotranspiration and a decrease in albedo (He et
555 al., 2017). Various bloom events in arid and semi-arid regions, such as rare blooms in the arid
556 Atacama Desert or superblooms of wildflowers in California's southeastern deserts, have
557 fascinated many researchers and media sources recently (Chávez et al., 2019; Martínez-Harms et
558 al., 2022; Winkler and Brooks, 2020). Our workflow could be useful for detecting and
559 monitoring such events, as well as for managing invasive plant species in grassland ecosystems.
560 Effective management strategies can help mitigate the impact of these invasive species,
561 promoting the health and resilience of grassland ecosystems.

562 The occurrence of sweetclover years is predominantly associated with wetter conditions,
563 suggesting that precipitation plays a key role in the resurgence of MEOF. We refer to those years
564 with mass blooming of MEOF in the Dakota region as "sweetclover years". They occurred only
565 during wetter years, when mass blooming cover followed higher than average precipitation
566 (Gucker, 2009). Despite this, However, climate variables like such as annual precipitation or
567 snow depth, did not rank among the top predicting variables. This may be due to MEOF's
568 biennial life cycle, where precipitation from the previous year can influence current-year cover
569 (Klebesadel, 1992; Van Riper and Larson, 2009). We tested this by including biennial
570 precipitation (MAP2). However, due to its high correlation with annual precipitation (MAP) and
571 the higher relative importance of MAP, neither variable alone, at the coarser 1 km resolution,
572 adequately captured the biennial dynamics. This unexpected result may be due to the large
573 disparity in spatial resolution between Sentinel-derived variables at 10 m and the 1 km climate
574 variables, which likely with the 10,000-fold difference in spatial resolution contributed to an
575 underestimation of precipitation's importance in the model as a significant variable. (Latimer et
576 al., 2006). There is a possibility that MEOF blooms could be influenced not just by precipitation
577 but also by local groundwater availability or soil moisture, particularly in areas near floodplains.
578 While we observed some higher cover near floodplain regions in certain years, the pattern was
579 not consistent across all years. Future analyses focusing on watersheds and hydrological
580 variables could help clarify the environmental drivers of bloom events. Overall, our findings
581 suggest that climate contributes to interannual variation in MEOF cover, while previous studies
582 suggest that spatial heterogeneity and local environmental conditions further modulate vegetation
583 dynamics across the Northern Great Plains (Fore, 2024). Therefore, we created a MEOF percent
584

Formatted: Font color: Auto

585 cover map series for 2016 through 2023 and compared it with precipitation anomaly maps during
586 the same period computed using the Daymet dataset product. These precipitation anomaly maps
587 showed that the western SD witnessed above average precipitation in a few regions for 2018 and
588 2023 and most of the western SD for 2019 (Figure S4). The central and eastern counties in 2019
589 and central and southern counties in 2023 showed a greater range of MEOF covers showing
590 consistent pattern of MEOF resurgence with the return of wet conditions. Despite 2016 being
591 a relatively normal or slightly dry year, sweetclover cover remained moderate with less spatial
592 variability, indicating less widespread establishment. The widespread establishment of MEOF
593 could be seen increasing in 2018 with high CV of 0.5 and then its percent cover reached a peak
594 in the subsequent year of 2019. For the years 2020, 2021 and 2022, most regions experienced
595 average to below average rainfall conditions. During these years, MEOF percent cover reached
596 up to 50%, with the sharp drop in percent cover in 2021, where the maximum cover was only
597 43%. This showed drought conditions likely limit growth and establishment. The year 2020 and
598 2022 acted as transitional years, possible due to lagged ecological response. For dry years, the
599 majority of western SD predicted less than 50% cover.

600
601
602 Overall, we found a high percent cover range in the western counties of western SD including
603 Butte, Meade, Pennington, Custer, Fall River, Jackson, Bennet and Oglala Lakota counties.
604 Central regions showed fluctuating trends with moderate to high coverage in some years (e.g.,
605 2018, 2019, 2023) and relatively low in other years (e.g., 2020, 2021). In the eastern counties
606 (i.e., Corson, Dewey, and Stanley), we observed a relatively low percent cover range with <20%.
607 In this region, MEOF appeared to be more scattered and patchier with some local increases near
608 floodplains, which are situated at lower elevations and benefit from high moisture availability
609 especially in the years 2018 and 2019. During the summer fieldwork of 2022, we observed
610 MEOF predominantly in the first year of its life cycle and an ample cover of MEOF blooms in
611 the Butte County in the consecutive year, in huge patches to be captured by the drones. This
612 temporal pattern arises from the biennial growth period of MEOF. Additionally, we predicted
613 MEOF percent cover estimates for the year 2024 using our trained model (Figure S5). However,
614 this 2024 predictions has not yet been validated due to the unavailability of field data. Validation
615 of model performance for 2024 and subsequent years remains a key focus for future work.

616
617 Nevertheless, despite experiencing ample moisture in some areas in 2016 or 2018, the
618 'sweetclover year' super blooms mass blooming were limited only to 2019. This phenomenon
619 may be attributed to MEOF's biennial life cycle, which plays a significant role and acts as a lag
620 effect provided average or above average conditions persist (Van Riper and Larson, 2009). A
621 distinct drop in coverage is seen in the years of 2020 and 2021 across the south, with a recovery
622 in 2022–2023. During the summer fieldwork of 2022, we observed MEOF predominantly in the
623 first year of its life cycle and an ample cover of MEOF blooms in the Butte County in the
624 consecutive year, in huge patches to be captured by the drones. This temporal pattern arises from
625 the biennial growth period of MEOF. Moreover, MEOF with >40% percent cover was found in
626 mostly regions that received above-average precipitation during both dry and wet years,
627 highlighting the importance of moisture in regulating dominance. This aligns with previous

628 studies showing that sweetclover cover can fluctuate substantially from year to year, driven by
629 its biennial growth habit and strong germination response in years with high precipitation
630 (Turkington et al., 1978).² Though the RF model did not identify precipitation as the top variable,
631 time-series precipitation maps supported the hypothesis that 'sweetclover years' characterized by
632 high MEOF abundance may occur when sustained average or above average precipitation
633 conditions help maintain sufficient soil moisture levels, despite losses from evapotranspiration.
634 Although the RF model did not identify precipitation as the top predictor, our predicted MEOF
635 cover maps showed that years of high cover (e.g., 2018 and 2019) coincided with favorable
636 moisture conditions, whereas lower cover in 2020–2021 corresponded with drier years. This
637 pattern supports the hypothesis that 'sweetclover years' of high MEOF abundance occur when
638 favorable moisture conditions are maintained, allowing successful establishment and dominance
639 despite losses from evapotranspiration. These favorable moisture conditions likely facilitate the
640 successful establishment and dominance of MEOF across the Northern Great Plains rangelands,
641 consistent with broader patterns observed for invasive species in semi-arid rangelands (Brooks et
642 al., 2004; D'Antonio and Vitousek, 1992). Similar patterns have been observed for exotic annual
643 grasses such as Cheatgrass (*Bromus tectorum* L.), Red brome (*Bromus rubens* L.) or
644 Medusahead (*Taeniatherum caput-medusae* (L.) Nevski), which often increase under periods of
645 favorable precipitation (Chen and Weber, 2014; Dahal et al., 2023).³ Additionally, we predicted
646 MEOF percent cover estimates for the year 2024 using our trained model (Figure S5). However,
647 this 2024 prediction has not yet been validated due to the unavailability of field data. Validation
648 of model performance for 2024 and subsequent years remains a key focus for future work.

649 Formatted: Font: Not Italic

650 Our study offers a workflow for different plant species of annuals, biennials, or geophytes that
651 share dominance during the blooming events, displaying huge appearances in specific years with
652 differences of 4 to 10 weeks in their length and peak of the flowering period (Vidiella et al.,
653 1999). These blooms cause a sudden increase in annual net primary production, triggering
654 relevant changes in the ecosystem such as soil nitrogen content, temporary plant composition
655 modifications, attraction of predators, etc. (Jaksic, 2001), as well as changes in the local climate:
656 an increase in evapotranspiration and a decrease in albedo (He et al., 2017). Various bloom
657 events in arid and semi-arid regions, such as rare blooms in the arid Atacama Desert or
658 superblooms of wildflowers in California's southeastern deserts, have fascinated many
659 researchers and media sources recently (Chávez et al., 2019; Martínez Harms et al., 2022;
660 Winkler and Brooks, 2020). Our workflow could be useful for detecting and monitoring such
661 events, as well as for managing invasive plant species in grassland ecosystems. Effective
662 management strategies can help mitigate the impact of these invasive species, promoting the
663 health and resilience of grassland ecosystems.

664 Formatted: Space After: 0 pt

665 Formatted: Font: (Default) Times New Roman, 12 pt,
666 Ligatures: None

667 The comprehensive database developed for the invasive MEOF provides a critical foundation for
668 understanding its spatial-temporal invasion dynamics across western SD. The database facilitates
669 detailed analyses of spread dynamics, invasion pathways, and distributional hotspots, thereby
670 improving the ability to model present distribution patterns and project future range expansions
under diverse environmental conditions. It also offers a valuable resource for long-term
ecological monitoring and adaptive management of MEOF. Furthermore, [the database supports](#)

664 Formatted: Normal

665 Formatted: Font: (Default) Times New Roman, 12 pt

671 investigation of the ecological consequences of MEOF invasion. For example, MEOF's nitrogen-
672 fixing ability may alter soil nutrient dynamics, potentially facilitate its own dominance while
673 affect native plant communities. Increased MEOF cover could lead to declines in native species
674 richness, shifts in plant community composition, and changes in ecosystem processes such as
675 nutrient cycling and primary productivity, particularly in nitrogen-limited prairie ecosystems.
676 Understanding these impacts is critical for predicting long-term vegetation changes and
677 developing targeted management strategies. the dataset supports investigations into the
678 ecological consequences of invasion, including potential associations between MEOF cover and
679 declines in native species richness, particularly within nitrogen-limited prairie ecosystems.
680 Beyond immediate applications, this database contributes to a broader understanding of
681 community-level vegetation changes driven by nitrogen-fixing invasive species in grassland
682 environments.

683
684 4.2 Significance of predictor variables
685

686 -The variable importance results for MEOF reveals that Normalized Difference Moisture Index
687 (NDMI) is the most influential predictor, indicating that soil and vegetation moisture plays a
688 crucial role in supporting its invasion and growth (Figure S2). NDMI characterizes the water
689 stress level in plants (Gao, 1996), which has been used to monitor drought stress and vegetation
690 moisture content (Strashok et al., 2022). Proximity to roads (Dist_roads) emerged as the second
691 most important predictor, explaining the higher cover of MEOF near the roads and its dispersion
692 through road corridors, as MEOF was previously planted along roadsides for soil stabilization
693 (Gucker, 2009). These findings align well with those of Wurtz et al., (2010) who showed that
694 MEOF might have spread onto floodplains from roads, mines, and agricultural fields. This
695 pattern is also consistent with our field survey plots, where a higher percent cover of MEOF was
696 observed closer to roads compared to the interior of plots. Nevertheless, the importance of road
697 proximity should be interpreted cautiously, as greater sampling accessibility near roads may have
698 partially inflated its role in the model. We also found variability in Normalized Difference Water
699 Index (NDWIcv) indicating areas with fluctuating surface water availability may create
700 favourable conditions for MEOF establishment. Furthermore, most climatic variables, such as
701 snow depth, variability in snow depth, mean annual precipitation and Temperature (MAP and
702 MAT), and variability in mean annual precipitation (MAPcv), were found to be of relatively low
703 importance, likely because of their coarser spatial resolutions (500 m and 1 km). Overall, It could
704 also suggest that climate may set the broad suitability for MEOF but local moisture dynamics
705 and human disturbances may play more critical role in shaping MEOF invasion patterns. our
706 results suggest that local moisture dynamics, captured by NDMI and NDWIcv, and human
707 disturbances, reflected by proximity to roads, are stronger determinants of MEOF distribution at
708 fine spatial scales than coarser-resolution climatic variables (snow depth, MAP, MAT, and their
709 variability). Although climate may establish broad-scale suitability, our data indicate that MEOF
710 invasion patterns in western South Dakota are primarily influenced by local hydrological
711 conditions and human-mediated dispersal.

712
713 4.3 MEOF cover estimates for 2019
714

← Formatted: Normal

Formatted: Font: Not Bold

Formatted: Font: Not Bold

715 It is important to note that reducing the sample size from 22,972 to 11,235 due to high spatial
716 correlation did not substantially affect model performance. However, in comparison to (Saraf et
717 al., (2023), a much larger overall sample size was required to improve predictive accuracy. We
718 developed a single generalized RF model across all years (2016–2023) and applied it to predict
719 MEOF cover annually. Thus, while temporal imbalance in samples (e.g., more samples from
720 bloom years such as 2019 and 2023) influenced the overall distribution of training data, spatial
721 balance and adequate coverage across the full percent cover range were the most critical factors
722 for model accuracy. We found that increasing the sample size and ensuring a more balanced
723 distribution significantly improved model performance, raising R^2 from 0.55 (Saraf et al., 2023)
724 to 0.76. RMSE increased from 7% to 15%, reflecting the inclusion of a wider range of percent
725 cover values rather than insufficient sample size or overall imbalance. Saraf et al., (2023)
726 reported that their model underestimated high percent cover due to a limited sample size ($n =$
727 1,612). In contrast, our model utilized a larger and more evenly distributed sample ($n = 11,235$)
728 across years, improving predictive accuracy and the representation of extreme cover values.
729 These findings suggest that balanced sample sizes enhance both the predictive range and
730 accuracy of RF models, although temporal imbalance in certain years may still influence RMSE
731 and require further investigation. Moreover, it is noteworthy to highlight that it is difficult to
732 fully stratify samples temporally for a biennial species like MEOF, which remains dormant
733 during certain seasons and blooms only under specific environmental conditions. We compared
734 our predicted MEOF cover map with those of Saraf et al., (2023) for 2019. We found that
735 increasing the sample size and ensuring a more balanced distribution significantly improved our
736 model accuracy, raising R^2 from 0.55 to 0.76, though it also increased RMSE. Saraf et al. (2023)
737 noted that the model underestimated the percent cover range due to the limited sample size ($n =$
738 1,612) and the limited frequency of high percent cover observation samples. The study showed
739 that the RF model performed adequately with R^2 of 0.55 and RMSE of 7.49, even with a limited
740 sample size ($n = 1,612$). In contrast, current model utilized a larger and more balanced sample
741 size ($n = 11,235$) with a uniform frequency distribution across years. The increase in sample size
742 led to a significant improvement in model accuracy, raising R^2 but also increased RMSE from
743 7% to 15% due to the unbalanced sample distribution across years. This finding suggests that
744 balanced sample sizes have the potential to improve both the prediction range and accuracy of
745 the model, though further testing with unbalanced designs is needed to fully evaluate their
746 efficacy.

747 Both predicted maps exhibited similar spatial patterns, with higher MEOF cover observed in the
748 western SD counties, such as Butte and Pennington. However, our model predicted a full range
749 of 0-100% cover for 2019, in contrast to the limited range observed in Saraf et al., (2023). This
750 difference is particularly evident in the high MEOF probability areas of western SD rangelands,
751 as shown in Figure 5.

752
753 We conclude that Saraf et al., (2023) significantly underestimated the extent of high percent
754 cover, reporting that areas with > 50% MEOF cover constituted only about 0.76% of SD's total
755 rangelands. In contrast, our updated prediction model estimated that ~12.6% (10,256 km²) of the
756 total rangeland area (81,442 km²) had >50% MEOF cover in 2019. The increase in sample size
757 improved the model ability to predict a wider range of percent cover, providing a more accurate
758 representation of the massive MEOF blooms across western SD in 2019.

760

Formatted: Font: Not Bold

Formatted: Font: Not Bold

Formatted: Font: Not Bold

Formatted: Font: Not Bold

761 4.4 Uncertainties

762
763 We manually delineated MEOF presence and absence polygons on the UAS imagery, which
764 were used to train and validate the RF classification model. The resulting classified image was
765 then used to derive continuous, wall-to-wall fractional cover estimates across the UAV sites. We
766 used these model-derived continuous MEOF cover values, rather than the manual polygons, for
767 regression analyses in order to generate numerous spatially explicit cover samples and to capture
768 gradients of invasion across the landscape. We manually delineated polygons of invasive MEOF
769 presence, which were then used to train the RF classifier. The UAS orthomosaics in a green-
770 blue-blue band false color combination helped to delineate training polygons. This approach
771 highlighted the potential of multi-spectral bands to easily detect MEOF patches. Furthermore, we
772 randomly sampled 6,000 pixels at 4-6 cm resolution corresponding to the presence and absence
773 of the invasive MEOF. ~~We~~ It was anticipated that errors might occur during the manual
774 delineation, although the RGB imagery employed in the study displayed the MEOF's
775 characteristic features, such as color, canopy shape, and flowers. The reliability of visual
776 delineation could be compromised in shaded areas. However, the RF classification could
777 accurately distinguish most MEOF pixels from non-MEOF pixels with 98.6%. Visual
778 inspections revealed no discrepancies between the derived percent cover maps at 10 m resolution
779 and submeter resolution MEOF classified maps. This result suggests that any alignment errors
780 were likely minimal and did not significantly affect model accuracy at 10 m resolution especially
781 after calibration of the derived percent cover. While these results are specific to our study area in
782 the Northern Great Plains, the approach has broader implicationspotential. We also produced a
783 predictive map for the year 2024 ([Figure S5](#)) using the trained model. Assessing the accuracy of
784 the 2024 predictions and extending validation to upcoming future years constitutes an important
785 direction for continued research. Our workflow combined with high-resolution UAS imagery and
786 machine learning can be adapted to other regions with similar vegetation structure and invasion
787 dynamics, offering a scalable and efficient tool for detecting and mapping invasive biennials like
788 MEOF across diverse rangeland ecosystems. Our approach of scaling UAS-derived observations
789 to develop percent cover estimates at broader spatial scales is conceptually similar to ([Rigge et](#)
790 [al., \(2020\)](#), who demonstrated the utility of integrating high-resolution reference data to improve
791 landscape-scale predictions of rangeland vegetation cover.

792
793 Formatted: Font: Not Bold

794
795 Formatted: Font: Not Bold

796 4.5 Validation for 2023 estimates

797 We validated the predicted MEOF cover maps using four independent UAS-validation sites.
798 Predictions showed strong correlation with observed MEOF cover derived from UAS imagery,
799 with an R^2 of 0.71, RMSE of 17.81%, MAE of 13.17%, and MAPE of 4.89% ([Figure 6, Figure](#)
800 [S6](#)). The visual comparison of the predicted maps with UAS imagery at the four validation sites
801 showed that the model generally captured the spatial patterns of MEOF cover. We found that the
802 prediction model underestimated the high percent cover range and overestimated the low to no
803 percent cover regions. In 2023, only 0.76% (621.4 km²) of the total rangeland area (81,442 km²)
804 showed cover exceeding 50%, supporting field observations of widespread MEOF blooms in
805 specific regions. The prominent yellow blooms of MEOF are readily visible in UAS and satellite
806 imagery when found in adequately big clusters, hence supporting the reliability of the model
predictions. We validated the predicted MEOF cover map with the remaining four UAS-
807 validation sites and found that the predictions exhibited high correlation with the observed

807 MEOF in the UAS imagery (Figure 6). Figure 6 shows the four validation sites in the green-
808 green-blue false color composite along with the predicted yellow sweetclover percent cover at 10
809 m resolution. The validation sites showed a good correspondence between the predicted percent
810 cover and the derived percent cover with R^2 of 0.71, RMSE of 17.81%, MAE of 13.17, and
811 MAPE of 4.89% (Figure S6). We found that the prediction model underestimated the high
812 percent cover range and overestimated the low to no percent cover regions. The prediction map
813 for 2023 revealed higher cover in the western counties, such as Butte, Harding, and Pennington
814 counties. We found that only 0.76 % (621.4 km^2) of the total rangeland area ($81,442 \text{ km}^2$)
815 exhibited cover above 50% in 2023. During our summer fieldwork, we observed yellow
816 sweetclover (MEOF) cover extensive enough to be effectively captured by drone flights in these
817 regions. MEOF has a prominent yellow flower that is distinctly visible in UAS and satellite
818 imagery, provided the blooms appear cover in larger patches enough to be visible in the
819 respective resolutions. Numerous previous remote sensing studies of invasive species have used
820 binary (presence/absence) classification approaches to map invasive species (Bradley, 2014b).
821 We chose to map the MEOF on an ordinal scale as this approach offers a measure of invasion
822 intensity at a larger landscape scale. We assert that assessing MEOF cover across the region can
823 help better evaluate the economic and ecological impacts of this invasive plant species.

824
825
826

827 In addition to UAS validation, we used four-band (visible and near-infrared), 3 m resolution
828 Dove Classic and SuperDove PlanetScope (PS) imagery for 2019 and 2023 through the NASA
829 CSDA program (Planet Labs PBC, 2023) to further assess model predictions (Figure 7). PS
830 scenes were selected for locations with predicted high MEOF cover, and false-color
831 combinations (green-green-blue) were applied to enhance visualization of MEOF blooms. These
832 imagery data offered an independent and freely available means to complement the UAS-based
833 validation by visually verifying the spatial patterns of predicted MEOF cover across sites where
834 field data were unavailable. In general, the validation results indicate that the RF model
835 effectively depicts spatial variation in MEOF cover throughout the study area, thereby providing
836 a reliable foundation for evaluating invasion intensity on a landscape scale. 4.6 Validation with
837 PlanetScope Imagery

838

839 We downloaded four band (visible and near infrared), 3 m resolution Dove Classic and
840 SuperDove PlanetScope (PS) imagery for 2019 and 2023 using our access to the NASA
841 Commercial SmallSat Data Acquisition (CSDA) program to validate our prediction maps (Planet
842 Labs PBC, 2023). We acquired PS scenes at four different locations with high percent cover field
843 sample points for 2019 and high MEOF cover predicted in 2019 and 2023 percent cover maps.
844 We again found that the false color combination of green-green-blue worked well to visualize
845 MEOF blooms. We observed that the intensity of MEOF flowering at the full bloom stage was
846 also discernible through PS imagery for 2019 and 2023, confirming the presence of MEOF in
847 these selected regions during the high MEOF cover years (Figure 7). We found that each site in
848 2023 exhibited a similar yellow reflectance of MEOF as observed in 2019. This result confirms
849 that our generalized model accurately predicted the presence of MEOF in sites where we did not
850 have field samples for 2023.

851

852 4.67 Limitations

853

854 Our model does not explicitly incorporate the biennial life cycle of MEOF; rather, we capture
 855 this variation indirectly by generating annual time-series maps (2016–2023) that reflect
 856 differences in cover between bloom and non-bloom years. Most of the observed MEOF cover
 857 samples were collected during the second year of its life cycle to enable capture of its flowering
 858 stage. Our model does not explain the variation in the MEOF cover that has biennial life cycle.
 859 Therefore, we aimed at mapping MEOF blooms or when MEOF was at flowering stage. Most of
 860 the observed MEOF cover samples were collected during the second year of its life cycle to
 861 enable capture of its flowering stage. The yellow sweetclover cover peaked during the wetter
 862 years (2019 and 2023) as shown in Figure S3, and most of the sampling strength was obtained
 863 during these years (Table S1). We used the coefficient of variation to capture the temporal
 864 variation of the independent variables during summer (JJA). However, cloud cover of >above
 865 10% in the region remained the major limitation of this study. In certain cases, we also examined
 866 the Harmonized Landsat Sentinel-2 (HLS) product (Claverie et al., 2018), where the cloud free
 867 maximum seasonal composites were limited to a single image per season due to the scarcity of
 868 cloud free images. We resolved this issue by substituting the coefficient of variation with the
 869 standard deviation of the seasonal mean of the variable. Sentinel-2 data provides high temporal
 870 resolution, fast data provisioning, and computing infrastructure, making it easier for land
 871 managers to track invasive species in real-time. Our model demonstrated high variable
 872 importance of high-resolution variables performed better than climate variables due to their
 873 coarser resolution. This underperformance of coarser variables suggests the need for higher
 874 spatial resolution datasets in mapping invasive plant species. High-resolution mapping, even at
 875 Sentinel-2 (10 m) or PlanetScope (3 m) resolution, is complicated by the uneven spatial
 876 resolution of independent variables, making it more difficult to understand their relative roles in
 877 characterizing the niche of invasive species. Mapping at very high resolution, such as 3 m
 878 PlanetScope imagery, has its own limitations, including fewer spectral bands, lower radiometric
 879 calibration, and higher noise levels in vegetation indices, which can affect the accuracy of
 880 species-specific detection. High resolution mapping with uneven spatial resolution variables also
 881 makes it more difficult to understand the relative roles of environmental variables in
 882 characterizing the niche of invasive species.

883

884 5. Data availability

885

886 The developed invasive MEOF percent cover datasets are freely available at the figshare
 887 repository (Saraf et al., 2025)
 888 (<https://doi.org/10.6084/m9.figshare.29270759.v1>).
 889 The repository has two folders: the first folder named “resampled predicted cover maps”
 890 contains predicted percent cover maps of invasive yellow sweetclover resampled at 20m
 891 resolution due to size limitations. We can provide the original 10m resolution images upon
 892 request. Each file is saved in GeoTiff format in the Albers Conic Equal Area projection. Each
 893 file is saved with an acronym of ‘m’ for MEOF followed by an underscore and a year. Missing

Formatted: Space After: 0 pt

Formatted: Default Paragraph Font, Font: (Default)
 +Body (Calibri), 11 pt

894 data are represented by "No data". The other folder named "sample_code_and_data" contains the
895 R code and an exemplary sample data to predict the MEOF percent cover.

896
897 **6. Conclusions**
898

899 Our integrated approach combining high-resolution UAS imagery, RF classification and
900 regression models, and multi-year satellite and climatic data enabled the effective mapping and
901 monitoring of MEOF cover across western South Dakota. The models demonstrated strong
902 performance with high accuracy in both classification and regression tasks, validating the use of
903 drone-derived percent cover for landscape-scale predictions. The findings highlight the critical
904 role of local moisture availability, proximity to roads, and surface water variability in driving
905 MEOF invasion, while broader climatic variables played a comparatively limited role due to
906 their coarser resolution. Temporal maps revealed that MEOF expansion is closely linked to
907 wetter years, aligning with its biennial life cycle and reinforcing the concept of "sweetclover
908 years." The updated 2019 cover map was significantly improved from the previous estimates,
909 capturing a broader percent cover range and representing invasion hotspots. Validation using
910 2023 UAS sites and PlanetScope imagery further confirmed the model's reliability. PlanetScope
911 imagery provided an independent means to visually assess predicted MEOF cover in areas where
912 drone data are unavailable and served as a complementary source of validation. Our study
913 proposes a workflow of a generalized model that could be applicable to various plant species
914 annuals, biennials, and geophytes that exhibit episodic dominance during blooming events. Our
915 database on MEOF enables analysis of its invasion dynamics, supports predictive modeling of
916 current and future distributions, and informs long-term monitoring and management. It also
917 provides a foundation for assessing ecological impacts on native species and community
918 composition in nitrogen-poor grasslands. Our study also provides a valuable tool for detecting
919 and monitoring supereruptive blooming events and can support the management of invasive
920 plant species such as MEOF in grassland ecosystems. Effective management strategies informed
921 by these insights may help mitigate the ecological impacts of invasive species, thereby enhancing
922 the health and resilience of grassland environments.

923 **Code availability**

924 The codes used to produce the multitemporal MEOF maps are publicly available on figshare
925 repository (Saraf et al., 2025) (<https://doi.org/10.6084/m9.figshare.29270759.v1>).

926

927 **Author contributions**

928 SS – Conceptualization, Data Curation, Formal Analysis, Methodology, Software, Validation,
929 Visualization, and Writing – original draft, review and editing. RJ - Funding acquisition,
930 Project administration, Resources, Supervision, Conceptualization and Writing – review &
931 editing. VK – Data Curation, Visualization, Software, Writing – review and editing. KJ - Data
932 Curation, Writing review & editing. GH - Visualization, Writing – review and editing. JC -
933 Writing – review and editing. RL - Writing – review and editing.

934

935 **Acknowledgements**

936 We thank all the institutes, organizations, and developers of the various datasets for making their
937 products freely available. Our appreciation also goes to NASA Commercial SmallSat Data
938 Acquisition (CSDA) program for providing us access with PlanetScope Imagery. We would also
939 like to thank Michele Thornton for providing us Daymet data for 2024 way ahead of its release
940 for us to predict MEOF percent cover for 2024. We acknowledge various funding sources
941 including NSF EPSCoR RII: EPSCoR Research Fellows, SDBOR Competitive Research Grant,
942 and the Cable Grant Fellowship, Department of Biology, University of South Dakota. We
943 sincerely thank both anonymous referees for their constructive comments and suggestions, which
944 greatly helped improve the quality of this manuscript.

Formatted: Font color: Text 1

945
946 **Competing interests**

947 The contact author has declared that none of the authors has any competing interests.

948

949 **References**

950 Agnew, W., Uresk, D. W., and Hansen, R. M.: Flora and Fauna Associated with Prairie Dog
951 Colonies and Adjacent Ungrazed Mixed-grass Prairie in Western South Dakota,
952 <https://doi.org/10.2307/3899285>, 1986.

953 Alvarez-Taboada, F., Araújo-Paredes, C., and Julián-Pelaz, J.: Mapping of the Invasive Species
954 Hakea sericea Using Unmanned Aerial Vehicle (UAV) and WorldView-2 Imagery and an
955 Object-Oriented Approach, *Remote Sens.*, 9, 913, <https://doi.org/10.3390/rs9090913>, 2017.

956 Baena, S., Moat, J., Whaley, O., and Boyd, D.: Identifying species from the air: UAVs and the
957 very high resolution challenge for plant conservation, *PLoS One*, 12, e0188714,
958 <https://doi.org/10.1371/journal.pone.0188714>, 2017.

959 Barrett, B.: Snow Data Assimilation System (SNODAS) Data Products at NSIDC, Version 1,
960 Center, Natl. Oper. Hydrol. Remote Sens., <https://doi.org/10.7265/N5TB14TC>, 2004.

961 Baumann, E., Beierkuhnlein, C., Preitauer, A., Schmid, K., and Rudner, M.: Evaluating remote
962 sensing data as a tool to minimize spatial autocorrelation in in-situ vegetation sampling,
963 *Erdkunde*, 79, 25–40, <https://doi.org/10.3112/erdkunde.2025.01.02>, 2025.

964 Bernath-Plaisted, J. S., Ribic, C. A., Hills, W. B., Townsend, P. A., and Zuckerberg, B.:
965 Microclimate complexity in temperate grasslands: implications for conservation and
966 management under climate change, *Environ. Res. Lett.*, 18, <https://doi.org/10.1088/1748-9326/acad4d3>, 2023.

967 Bradley, B. A.: Remote detection of invasive plants: a review of spectral, textural and
968 phenological approaches, *Biol. Invasions*, 16, 1411–1425, <https://doi.org/10.1007/s10530-013-0578-9>, 2014.

969 Breiman, L.: *Classification and regression trees*, Routledge, 2017.

970 Breiman, L., Friedman, J. H., Olshen, R. A., and Stone, C. ..: *Classification And Regression*
971 *Trees* (1st ed.), Routledge, <https://doi.org/https://doi.org/10.1201/9781315139470>, 1984.

972 Brooks, M. L., D'Antonio, C. M., Richardson, D. M., Grace, J. B., Keeley, J. E., DiTomaso, J.
973 M., Hobbs, R. J., Pellatt, M., and Pyke, D.: Effects of invasive alien plants on fire regimes,
974 *Bioscience*, 54, 677–688, [https://doi.org/10.1641/0006-3568\(2004\)054\[0677:EOIAPO\]2.0.CO;2](https://doi.org/10.1641/0006-3568(2004)054[0677:EOIAPO]2.0.CO;2),
975 2004.

976 Chaney, N. W., Minasny, B., Herman, J. D., Nauman, T. W., Brungard, C. W., Morgan, C. L. S.,
977 McBratney, A. B., Wood, E. F., and Yimam, Y.: POLARIS Soil Properties: 30-m Probabilistic
978 Maps of Soil Properties Over the Contiguous United States, *Water Resour. Res.*, 55, 2916–2938,
979 <https://doi.org/10.1029/2018WR022797>, 2019.

982 Chávez, R. O., Moreira-Muñoz, A., Galleguillos, M., Olea, M., Aguayo, J., Latín, A., Aguilera-
983 Betti, I., Muñoz, A. A., and Manríquez, H.: GIMMS NDVI time series reveal the extent,
984 duration, and intensity of “blooming desert” events in the hyper-arid Atacama Desert, Northern
985 Chile, *Int. J. Appl. Earth Obs. Geoinf.*, 76, 193–203,
986 <https://doi.org/https://doi.org/10.1016/j.jag.2018.11.013>, 2019.

987 Chen, F. and Weber, K. T.: Assessing the impact of seasonal precipitation and temperature on
988 vegetation in a grass-dominated rangeland, *Rangel. J.*, 36, 185–190, 2014.

989 Cleland, E. E., Collins, S. L., Dickson, T. L., Farrer, E. C., Gross, K. L., Gherardi, L. A., Hallett,
990 L. M., Hobbs, R. J., Hsu, J. S., Turnbull, L., and Suding, K. N.: Sensitivity of grassland plant
991 community composition to spatial vs. temporal variation in precipitation, *Ecology*, 94, 1687–
992 1696, <https://doi.org/https://doi.org/10.1890/12-1006.1>, 2013.

993 Colomina, I. and Molina, P.: Unmanned aerial systems for photogrammetry and remote sensing:
994 A review, *ISPRS J. Photogramm. Remote Sens.*, 92, 79–97,
995 <https://doi.org/https://doi.org/10.1016/j.isprsjprs.2014.02.013>, 2014.

996 D'Antonio, C. M. and Vitousek, P. M.: Biological Invasions by Exotic Grasses, the Grass/Fire
997 Cycle, and Global Change, *Annu. Rev. Ecol. Syst.*, 23, 63–87, 1992.

998 Dahal, D., Boyte, S. P., and Oimoen, M. J.: Predicting Exotic Annual Grass Abundance in
999 Rangelands of the Western United States Using Various Precipitation Scenarios, *Rangel. Ecol.*
1000 *Manag.*, 90, 221–230, <https://doi.org/https://doi.org/10.1016/j.rama.2023.04.011>, 2023.

1001 Dewitz, J.: National Land Cover Database (NLCD) 2019 Products, US Geol. Surv. Sioux Falls,
1002 SD, USA, <https://doi.org/https://doi.org/10.5066/P9KZCM54>, 2021.

1003 Dubuis, A., Pottier, J., Rion, V., Pellissier, L., Theurillat, J. P., and Guisan, A.: Predicting spatial
1004 patterns of plant species richness: A comparison of direct macroecological and species stacking
1005 modelling approaches, *Divers. Distrib.*, 17, 1122–1131, <https://doi.org/10.1111/j.1472-4642.2011.00792.x>, 2011.

1006 Fore, S. R.: The Impact of Land Use and Land Cover Change on Vegetation, Ecosystem
1007 Dynamics, and Conservation in the Northern Great Plains, The University of North Dakota PP -
1008 United States -- North Dakota, United States -- North Dakota, 493 pp., 2024.

1009 Gao, B.: NDWI—A normalized difference water index for remote sensing of vegetation liquid
1010 water from space, *Remote Sens. Environ.*, 58, 257–266,
1011 [https://doi.org/https://doi.org/10.1016/S0034-4257\(96\)00067-3](https://doi.org/https://doi.org/10.1016/S0034-4257(96)00067-3), 1996.

1012 Gascon, F., Bouzinac, C., Thépaut, O., Jung, M., Francesconi, B., Louis, J., Lonjou, V.,
1013 Lafrance, B., Massera, S., Gaudel-Vacaresse, A., Languille, F., Alhammoud, B., Viallefond, F.,
1014 Pflug, B., Bieniarz, J., Clerc, S., Pessiot, L., Trémas, T., Cadau, E., De Bonis, R., Isola, C.,
1015 Martimort, P., and Fernandez, V.: Copernicus Sentinel-2A calibration and products validation
1016 status, *Remote Sens.*, 9, <https://doi.org/10.3390/rs9060584>, 2017.

1017 Gaskin, J. F., Espeland, E., Johnson, C. D., Larson, D. L., Mangold, J. M., McGee, R. A.,
1018 Milner, C., Paudel, S., Pearson, D. E., Perkins, L. B., Prosser, C. W., Runyon, J. B., Sing, S. E.,
1019 Sylvain, Z. A., Symstad, A. J., and Tekiela, D. R.: Managing invasive plants on Great Plains
1020 grasslands: A discussion of current challenges, *Rangel. Ecol. Manag.*, 78, 235–249,
1021 <https://doi.org/10.1016/j.rama.2020.04.003>, 2021.

1022 Gränzig, T., Fassnacht, F. E., Kleinschmit, B., and Förster, M.: Mapping the fractional coverage
1023 of the invasive shrub *Ulex europaeus* with multi-temporal Sentinel-2 imagery utilizing UAV
1024 orthoimages and a new spatial optimization approach, *Int. J. Appl. Earth Obs. Geoinf.*, 96,
1025 <https://doi.org/10.1016/j.jag.2020.102281>, 2021.

1026 Gucker, C. L.: *Melilotus alba*, *M. officinalis*, U.S. Dep. Agric. For. Serv. Rocky Mt. Res. Station.

1027

1028 Fire Sci. Lab., 2009.

1029 Guyon, I., Weston, J., Barnhill, S., and Vapnik, V.: Gene Selection for Cancer Classification
1030 using Support Vector Machines, *Mach. Learn.*, 46, 389–422,
1031 <https://doi.org/10.1023/A:1012487302797>, 2002.

1032 He, B., Huang, L., Liu, J., Wang, H., Lü, A., Jiang, W., and Chen, Z.: The observed cooling
1033 effect of desert blooms based on high-resolution Moderate Resolution Imaging
1034 Spectroradiometer products, *Earth Sp. Sci.*, 4, 247–256,
1035 <https://doi.org/https://doi.org/10.1002/2016EA000238>, 2017.

1036 Hendrickson, J. R., Sedivec, K. K., Toledo, D., and Printz, J.: Challenges Facing Grasslands
1037 in the Northern Great Plains and North Central Region, *Rangelands*, 41, 23–29,
1038 <https://doi.org/https://doi.org/10.1016/j.rala.2018.11.002>, 2019.

1039 Horstrand, P., Guerra, R., Rodríguez, A., Díaz, M., López, S., and López, J. F.: A UAV Platform
1040 Based on a Hyperspectral Sensor for Image Capturing and On-Board Processing, *IEEE Access*,
1041 7, 66919–66938, <https://doi.org/10.1109/ACCESS.2019.2913957>, 2019.

1042 Jaksic, F. M.: Ecological effects of El Niño in terrestrial ecosystems of western South America,
1043 *Ecography* (Cop.), 24, 241–250, <https://doi.org/https://doi.org/10.1111/j.1600-0587.2001.tb00196.x>, 2001.

1044 John, R., Chen, J., Giannico, V., Park, H., Xiao, J., Shirkey, G., Ouyang, Z., Shao, C.,
1045 Laforteza, R., and Qi, J.: Grassland canopy cover and aboveground biomass in Mongolia and
1046 Inner Mongolia: Spatiotemporal estimates and controlling factors, *Remote Sens. Environ.*, 213,
1047 34–48, <https://doi.org/10.1016/j.rse.2018.05.002>, 2018.

1048 Johnson, J. R. and Larson, G. E.: Grassland Plants of South Dakota and the Northern Great
1049 Plains, *Research Bulletins of the South Dakota Agricultural Experiment Station* (1887–2011),
1050 764 pp., 1999.

1051 Josso, P., Hall, A., Williams, C., Le Bas, T., Lusty, P., and Murton, B.: Application of random-
1052 forest machine learning algorithm for mineral predictive mapping of Fe-Mn crusts in the World
1053 Ocean, *Ore Geol. Rev.*, 162, 105671,
1054 <https://doi.org/https://doi.org/10.1016/j.oregeorev.2023.105671>, 2023.

1055 Jurjević, L., Gašparović, M., Milas, A. S., and Balenović, I.: Impact of UAS Image Orientation
1056 on Accuracy of Forest Inventory Attributes, *Remote Sens.*, 12,
1057 <https://doi.org/10.3390/rs12030404>, 2020.

1058 Kan, H., Teng, W., Chen, C., Zhang, G., and Pang, Z.: Establishment of alien invasive plant,
1059 yellow sweet clover (*Melilotus officinalis*) at a complex ecosystem distributed with farmlands
1060 and wasted lands, <https://doi.org/10.21203/rs.3.rs-2933552/v1>, 2023.

1061 Kattenborn, T., Lopatin, J., Förster, M., Braun, A. C., and Fassnacht, F. E.: UAV data as
1062 alternative to field sampling to map woody invasive species based on combined Sentinel-1 and
1063 Sentinel-2 data, *Remote Sens. Environ.*, 227, 61–73,
1064 <https://doi.org/https://doi.org/10.1016/j.rse.2019.03.025>, 2019.

1065 Klebesadel, L. J.: Extreme Northern Acclimatization in Biennial Yellow Sweetclover (*Melilotus*
1066 *officinalis*) at the Arctic Circle, *School of Agriculture and Land Resources Management*,
1067 *Agricultural and Forestry Experiment Station*, 1992.

1068 Kuhn, M.: A Short Introduction to the caret Package, *R Found. Stat. Comput.*, 1–10, 2015.

1069 Landis, J. R. and Koch, G. G.: The Measurement of Observer Agreement for Categorical Data,
1070 *Biometrics*, 33, 159, <https://doi.org/10.2307/2529310>, 1977.

1071 Langholz, J.: Global Trends in Private Protected Areas and their Implications for the Northern
1072 Great Plains Source: Great Plains, *Gt. Plains Res.*, 20, 9–16, 2010.

1073

1074 Larson, E. R., Graham, B. M., Achury, R., Coon, J. J., Daniels, M. K., Gambrell, D. K., Jonasen,
1075 K. L., King, G. D., LaRacuente, N., Perrin-Stowe, T. I. N., Reed, E. M., Rice, C. J., Ruzi, S. A.,
1076 Thairu, M. W., Wilson, J. C., and Suarez, A. V: From eDNA to citizen science: emerging tools
1077 for the early detection of invasive species, *Front. Ecol. Environ.*, 18, 194–202,
1078 <https://doi.org/https://doi.org/10.1002/fee.2162>, 2020.

1079 Latimer, A. M., Wu, S., Gelfand, A. E., and Silander Jr., J. A.: Building Statistical Models To
1080 Analyze Species Distributions, *Ecol. Appl.*, 16, 33–50, <https://doi.org/https://doi.org/10.1890/04-0609>, 2006.

1081 Li, L.-Y. and Tsai, C.-C.: Assessing online learning material: Quantitative behavior patterns and
1082 their effects on motivation and learning performance, *Comput. Educ.*, 114,
1083 <https://doi.org/10.1016/j.compedu.2017.07.007>, 2017.

1084 Liu, X., Kounadi, O., and Zurita-Milla, R.: Incorporating Spatial Autocorrelation in Machine
1085 Learning Models Using Spatial Lag and Eigenvector Spatial Filtering Features,
1086 <https://doi.org/10.3390/ijgi11040242>, 2022.

1087 Luo, K., Jahufer, M. Z. Z., Wu, F., Di, H., Zhang, D., Meng, X., Zhang, J., and Wang, Y.:
1088 Genotypic variation in a breeding population of yellow sweet clover (*Melilotus officinalis*),
1089 *Front. Plant Sci.*, 7, 1–10, <https://doi.org/10.3389/fpls.2016.00972>, 2016.

1090 Martínez-Harms, J., Guerrero, P., Martínez-Harms, M., Poblete, N., González, K., Stavenga, D.,
1091 and Vorobyev, M.: Mechanisms of flower coloring and eco-evolutionary implications of massive
1092 blooming events in the Atacama Desert, *Front. Ecol. Evol.*, 10,
1093 <https://doi.org/10.3389/fevo.2022.957318>, 2022.

1094 Martins, J., Richardson, D. M., Henriques, R., Marchante, E., Marchante, H., Alves, P., Gaertner,
1095 M., Honrado, J. P., and Vicente, J. R.: A multi-scale modelling framework to guide management
1096 of plant invasions in a transboundary context, *For. Ecosyst.*, 3, <https://doi.org/10.1186/s40663-016-0073-8>, 2016.

1097 Mayr, S., Kuenzer, C., Gessner, U., Klein, I., and Rutzinger, M.: Validation of Earth Observation
1098 Time-Series: A Review for Large-Area and Temporally Dense Land Surface Products, *Remote
1099 Sens.*, 11, 2616, <https://doi.org/10.3390/rs11222616>, 2019.

1100 Moran, P. A. P.: Notes on Continuous Stochastic Phenomena, *Biometrika*, 37(2), 17–29, 1950.

1101 Mouta, N., Silva, R., Pinto, E. M., Vaz, A. S., Alonso, J. M., Gonçalves, J. F., Honrado, J., and
1102 Vicente, J. R.: Sentinel-2 Time Series and Classifier Fusion to Map an Aquatic Invasive Plant
1103 Species along a River—The Case of Water-Hyacinth, *Remote Sens.*, 15,
1104 <https://doi.org/10.3390/rs15133248>, 2023.

1105 Müllerová, J., Brůna, J., Bartaloš, T., Dvořák, P., Vítková, M., and Pyšek, P.: Timing Is
1106 Important: Unmanned Aircraft vs. Satellite Imagery in Plant Invasion Monitoring, *Front. Plant
1107 Sci.*, 8, 1–13, <https://doi.org/10.3389/fpls.2017.00887>, 2017.

1108 Owensby, C. E. and Launchbaugh, J. L.: Controlling prairie threeawn (*Aristida oligantha*
1109 *Michx.*) in central and eastern Kansas with fall burning, *J. Range Manag.*, 30, 337–339, 1977.

1110 Padró, J.-C., Muñoz, F.-J., Planas, J., and Pons, X.: Comparison of four UAV georeferencing
1111 methods for environmental monitoring purposes focusing on the combined use with airborne and
1112 satellite remote sensing platforms, *Int. J. Appl. Earth Obs. Geoinf.*, 75, 130–140,
1113 <https://doi.org/https://doi.org/10.1016/j.jag.2018.10.018>, 2019.

1114 Paul, M., Rajib, A., and Ahiablame, L.: Spatial and Temporal Evaluation of Hydrological
1115 Response to Climate and Land Use Change in Three South Dakota Watersheds, *JAWRA J. Am.
1116 Water Resour. Assoc.*, 53, <https://doi.org/10.1111/1752-1688.12483>, 2016.

1117 Pix4D S.A.: Pix4Dmapper. Version 4.8, www.pix4d.com, 2022.

1120 Preston, T. M., Johnston, A. N., Ebenhoch, K. G., and Diehl, R. H.: Beyond presence mapping:
1121 predicting fractional cover of non-native vegetation in Sentinel-2 imagery using an ensemble of
1122 MaxEnt models, *Remote Sens. Ecol. Conserv.*, 9, 512–526, <https://doi.org/10.1002/rse2.325>,
1123 2023.

1124 Rai, P. and Singh, J. S.: Invasive alien plant species: Their impact on environment, ecosystem
1125 services and human health, *Ecol. Indic.*, 2020, 20 pages,
1126 <https://doi.org/10.1016/j.ecolind.2019.106020>, 2020.

1127 Rakotoarivony, M. N. A., Gholizadeh, H., Hammond, W. M., Hassani, K., Joshi, O., Hamilton,
1128 R. G., Fuhlendorf, S. D., Trowbridge, A. M., and Adams, H. D.: Detecting the invasive
1129 *Lespedeza cuneata* in grasslands using commercial small satellite imagery, *Int. J. Remote Sens.*,
1130 44, 6802–6824, <https://doi.org/10.1080/01431161.2023.2275321>, 2023.

1131 Van Rees, C. B., Hand, B. K., Carter, S. C., Bargeron, C., Cline, T. J., Daniel, W., Ferrante, J.
1132 A., Gaddis, K., Hunter, M. E., Jarnevich, C. S., McGeoch, M. A., Morisette, J. T., Neilson, M.
1133 E., Roy, H. E., Rozance, M. A., Sepulveda, A., Wallace, R. D., Whited, D., Wilcox, T., Kimball,
1134 J. S., and Luikart, G.: A framework to integrate innovations in invasion science for proactive
1135 management, *Biol. Rev.*, 97, 1712–1735, <https://doi.org/10.1111/brv.12859>, 2022.

1136 Reinhart, K. O., Rinella, M. J., Waterman, R. C., Petersen, M. K., and Vermeire, L. T.: Testing
1137 rangeland health theory in the Northern Great Plains, *J. Appl. Ecol.*, 56, 319–329, 2019.

1138 Rigge, M., Homer, C., Cleeves, L., Meyer, D. K., Bunde, B., Shi, H., Xian, G., Schell, S., and
1139 Bobo, M.: Quantifying Western U.S. Rangelands as Fractional Components with Multi-
1140 Resolution Remote Sensing and In Situ Data, <https://doi.org/10.3390/rs12030412>, 2020.

1141 Riggs, G. A., Hall, D. K., Román, M. O., and others: MODIS snow products collection 6 user
1142 guide, *Natl. Snow Ice Data Cent.* Boulder, CO, USA, 66, 2015.

1143 Van Riper, L. C. and Larson, D. L.: Role of invasive *Melilotus officinalis* in two native plant
1144 communities, *Plant Ecol.*, 200, 129–139, <https://doi.org/10.1007/s11258-008-9438-6>, 2009.

1145 Sanderson, M., Liebig, M., Hendrickson, J. R., Kronberg, S., Toledo, D., Derner, J., and Reeves,
1146 J.: Long-term agroecosystem research on northern Great Plains mixed grass prairie near Mandan,
1147 North Dakota, *Can. J. Plant Sci.*, 95, 150810114732003, <https://doi.org/10.4141/CJPS-2015-117>,
1148 2015.

1149 Saraf, S., John, R., Goljani Amirkhiz, R., Kolluru, V., Jain, K., Rigge, M., Giannico, V., Boyte,
1150 S., Chen, J., Henebry, G., Jarchow, M., and Laforteza, R.: Biophysical drivers for predicting the
1151 distribution and abundance of invasive yellow sweetclover in the Northern Great Plains, *Landsc.
1152 Ecol.*, 38, 1463–1479, <https://doi.org/10.1007/s10980-023-01613-1>, 2023.

1153 Saraf, S., John, R., Kolluru, V., Jain, K., Henebry, G., Chen, J., and Laforteza, R.:
1154 Spatiotemporal mapping of invasive yellow sweetclover blooms using Sentinel-2 and high-
1155 resolution drone imagery, <https://doi.org/10.6084/m9.figshare.29270759>, 2025.

1156 Spiess, J., McGranahan, D., Geaumont, B., Sedivec, K., Lakey, M., Berti, M., Hovick, T., and
1157 Limb, R.: Patch-Burning Buffers Forage Resources and Livestock Performance to Mitigate
1158 Drought in the Northern Great Plains, *Rangel. Ecol. Manag.*, 73,
1159 <https://doi.org/10.1016/j.rama.2020.03.003>, 2020.

1160 Steen, V. A., Tingley, M. W., Paton, P. W. C., and Elphick, C. S.: Spatial thinning and class
1161 balancing: Key choices lead to variation in the performance of species distribution models with
1162 citizen science data, *Methods Ecol. Evol.*, 12, 216–226,
1163 <https://doi.org/https://doi.org/10.1111/2041-210X.13525>, 2021.

1164 Stohlgren, T. J., Ma, P., Kumar, S., Rocca, M., Morisette, J. T., Jarnevich, C. S., and Benson, N.:
1165 Ensemble habitat mapping of invasive plant species, *Risk Anal.*, 30, 224–235,

1166 <https://doi.org/10.1111/j.1539-6924.2009.01343.x>, 2010.

1167 Strashok, O., Ziemiańska, M., and Strashok, V.: Evaluation and Correlation of Sentinel-2 NDVI
1168 and NDMI in Kyiv (2017-2021), *J. Ecol. Eng.*, 23, 212–218,
1169 <https://doi.org/10.12911/22998993/151884>, 2022.

1170 Sulik, J. J. and Long, D. S.: Spectral considerations for modeling yield of canola, *Remote Sens.*
1171 *Environ.*, 184, 161–174, <https://doi.org/10.1016/j.rse.2016.06.016>, 2016.

1172 Thornton, M. M., Shrestha, R., Wei, Y., Thornton, P. E., and Kao, S.-C.: Daymet: Monthly
1173 Climate Summaries on a 1-km Grid for North America, Version 4 R1,
1174 <https://doi.org/10.3334/ORNLDAA/2131>, 2022.

1175 Trimble Inc. (n.d.): Trimble DA2 GNSS Receiver,
1176 <https://geospatial.trimble.com/en/products/hardware/trimble-da2>, 2025.

1177 Turkington, R. A., Cavers, P. B., and Rempel, E.: *The Biology of Canadian Weeds*.: 29.

1178 *Melilotus alba* Desr. and *M. officinalis* (L.) Lam., *Can. J. Plant Sci.*, 58, 523–537,
1179 <https://doi.org/10.4141/cjps78-078>, 1978.

1180 Turner, D. and Wallace, L.: Direct Georeferencing of Ultrahigh-Resolution UAV Imagery, *IEEE*
1181 *Trans. Geosci. Remote Sens.*, 52, <https://doi.org/10.1109/TGRS.2013.2265295>, 2013.

1182 Varner, C.: *Invasive Flora of the West Coast: British Columbia and the Pacific Northwest*,
1183 Heritage House Publishing Co., University of Washington Press, 2022.

1184 Vidiella, P. E., Armesto, J. J., and Gutiérrez, J. R.: Vegetation changes and sequential flowering
1185 after rain in the southern Atacama Desert, *J. Arid Environ.*, 43, 449–458,
1186 <https://doi.org/10.1006/jare.1999.0565>, 1999.

1187 Winkler, D. E. and Brooks, E.: Tracing Extremes across Iconic Desert Landscapes: Socio-
1188 Ecological and Cultural Responses to Climate Change, *Water Scarcity, and Wildflower*
1189 *Superblooms*, *Hum. Ecol.*, 48, 211–223, <https://doi.org/10.1007/s10745-020-00145-5>, 2020.

1190 Wolf, J. J., Beatty, S. W., and Carey, G.: Invasion by Sweet Clover (*Melilotus*) in Montane
1191 Grasslands, *Rocky Mountain National Park, Ann. Assoc. Am. Geogr.*, 93, 531–543,
1192 <https://doi.org/10.1111/1467-8306.9303001>, 2003.

1193 Wolter, K. M.: The Jackknife Method BT - Introduction to Variance Estimation, edited by:
1194 Wolter, K. M., Springer New York, New York, NY, 151–193, https://doi.org/10.1007/978-0-387-35099-8_4, 2007.

1195 Wurtz, T. L., Macander, M. J., and Spellman, B. T.: Spread of Invasive Plants From Roads to
1196 River Systems in Alaska: A Network Model, *U S For. Serv. Pacific Northwest Res. Stn. Gen.*
1197 *Tech. Rep. PNW-GTR*, 699–708, 2010.

1198 Zar, J. H.: Spearman rank correlation, *Encycl. Biostat.* Wiley Online Libr., 7, 2005.

1199 Zhang, Z., Bao, T., Hautier, Y., Yang, J., Liu, Z., and Qing, H.: Microclimate complexity in
1200 temperate grasslands: implications for conservation and management under climate change,
1201 *Ecol. Evol.*, 12, e9385, <https://doi.org/10.1002/ece3.9385>, 2022.

1202

1203

1204 **Tables and Figures**

1205

1206

Table 1. Details of the drone flights covered in sample collection for summer 2023.

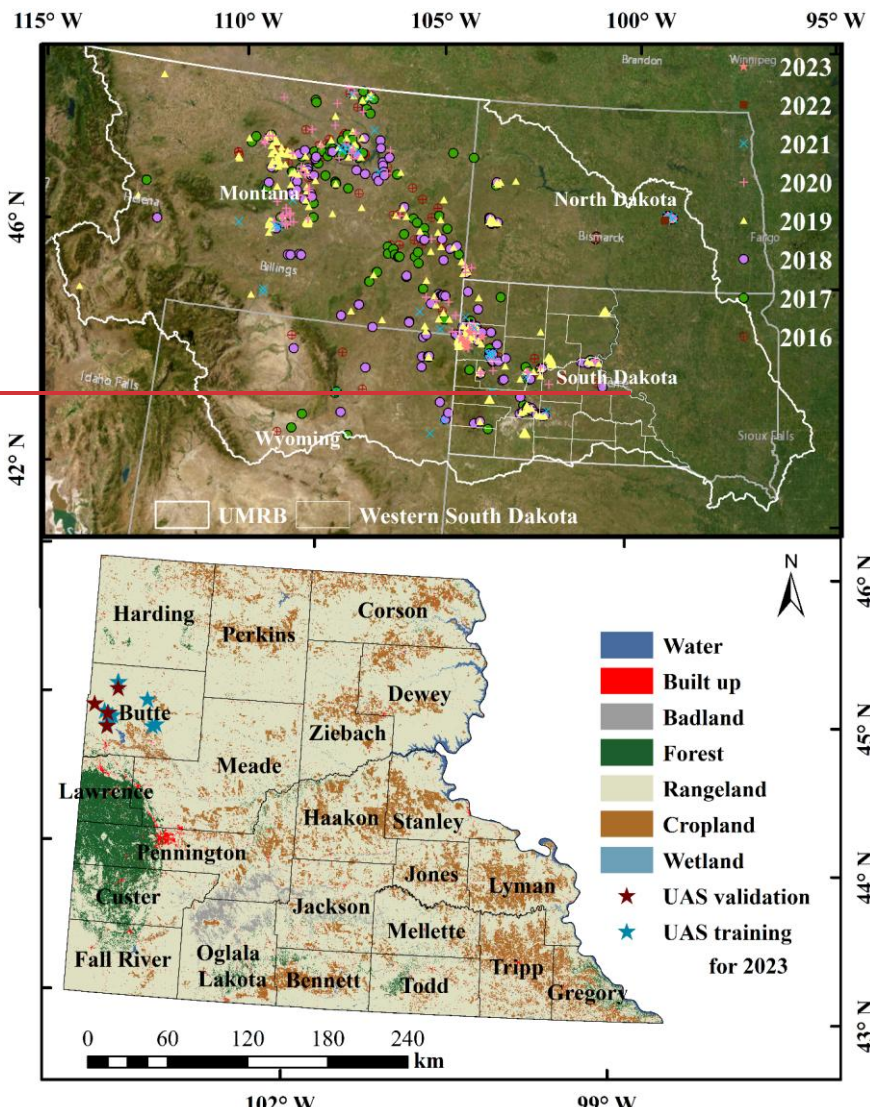
Site	Date	Spatial Resolution (m)	Area (ha)	Sampling
1	July 9	0.06	10.5	Validation
2	July 9	0.03	1.9	Training
3	July 10	0.04	4.9	Training
4	July 10	0.04	4.1	Training
5	July 11	0.07	30.5	Training
6	July 11	0.04	3.2	Training
7	July 12	0.05	7.2	Training
8	July 12	0.03	3	Training
9	July 13	0.04	4.9	Validation
10	July 13	0.04	4.6	Validation
11	July 14	0.03	4.2	Training
12	July 14	0.05	7.2	Training
13	July 15	0.05	10.5	Training
14	July 15	0.04	4.7	Validation

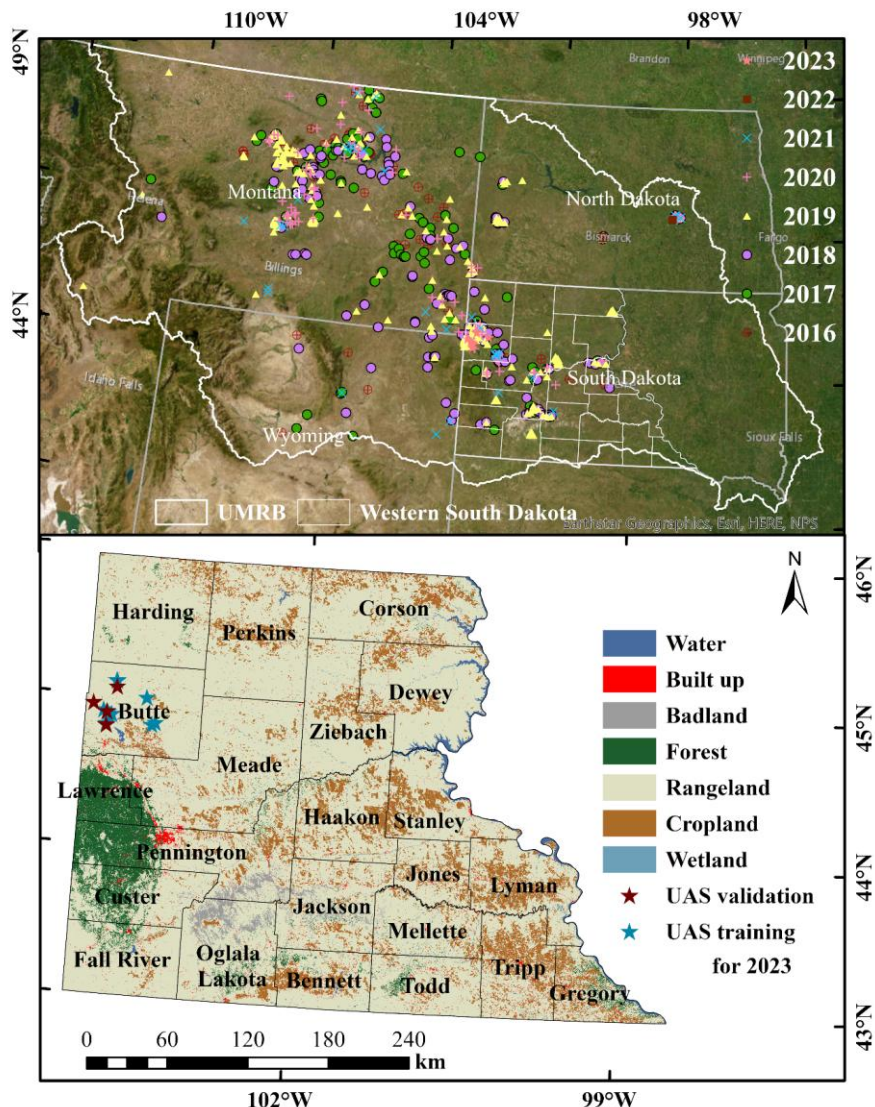
1207

1208 Table 2. Description of 13 independent variables selected for estimating the yellow sweetclover
1209 cover (%)

S.No	Independent Variables	Codes	Resolution
1	Mean annual precipitation	MAP	1 km
2	Mean annual precipitation (coefficient of variation)	MAPcv	1 km
3	Mean annual temperature	MAT	1 km
4	Mean annual precipitation (coefficient of variation)	MATcv	1 km
5	Snow Depth	SnowDepth	500m
6	Snow Depth (coefficient of variation)	SnowDepth_cv	500m
7	Elevation	Elevation	10m
8	Slope	Slope	10m
9	Proximity to roads	Dist_Roads	30m
10	Normalized Difference Moisture Index	NDMI	10m
11	Normalized Difference Water Index (coefficient of variation)	NDWIcv	10m
12	Land Surface Water Index (coefficient of variation)	LSWIcv	10m
13	Tasseled Cap Wetness (coefficient of variation)	TCWcv	10m

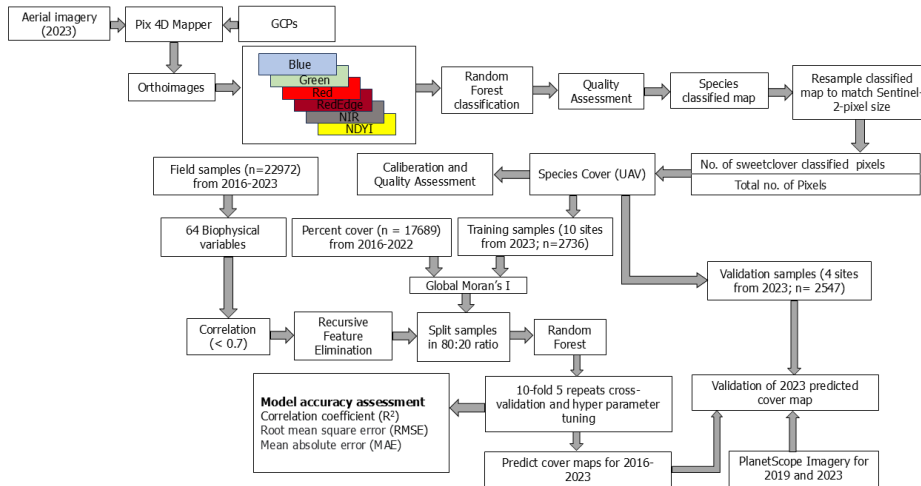
1210





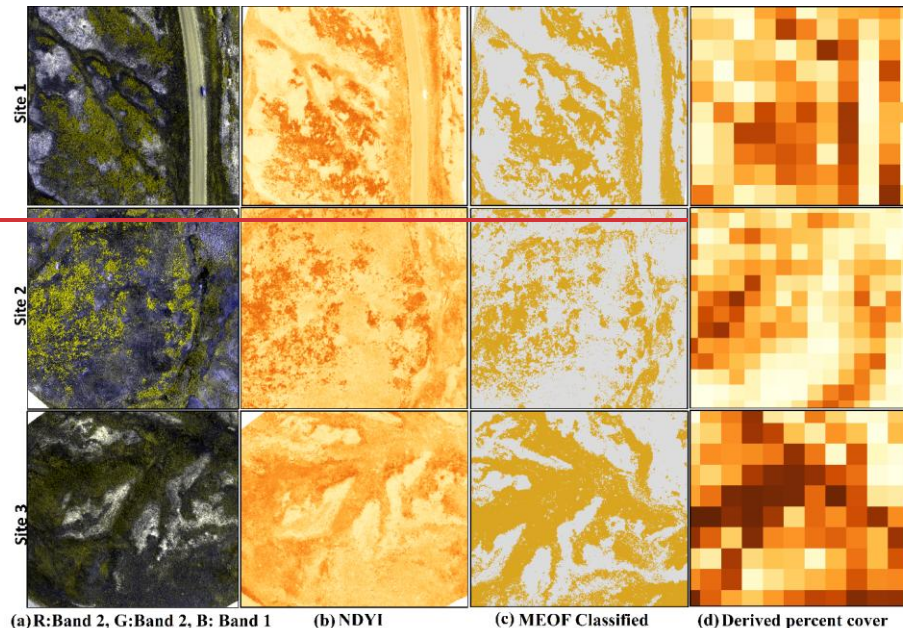
1212
1213 Figure 1 The top panel shows field observations used in this study (n = 22,972) collected from
1214 2016 to 2023 across the Northern Great Plains, including our own surveys as well as publicly
1215 available datasets such as BLM AIM and NEON (© Esri, Maxar, Earthstar Geographics, and the
1216 GIS User Community). The bottom panel shows the UAS training and validation sites overlaid
1217 on the National Land Cover Database (NLCD, 2019) land cover map with county boundaries of
1218 western South Dakota. The top panel shows the field data collected (n = 22,972) from 2016 to

1219 2023 across the Northern Great Plains (© Esri, Maxar, Earthstar Geographics, and the GIS User
1220 Community). The second panel shows the UAS training and validation sites overlaid on land
1221 cover map with county boundaries of western South Dakota.

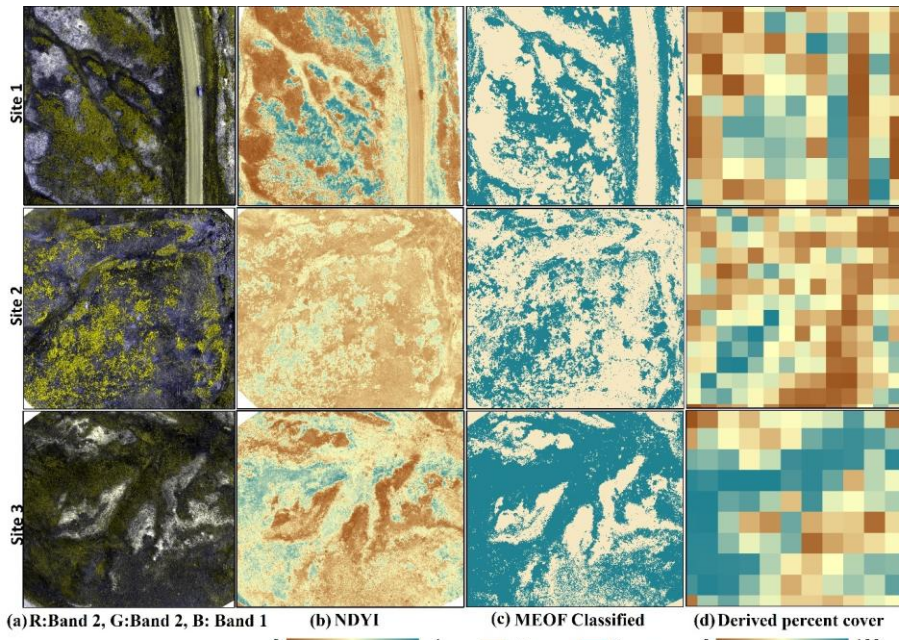


1222
1223
1224

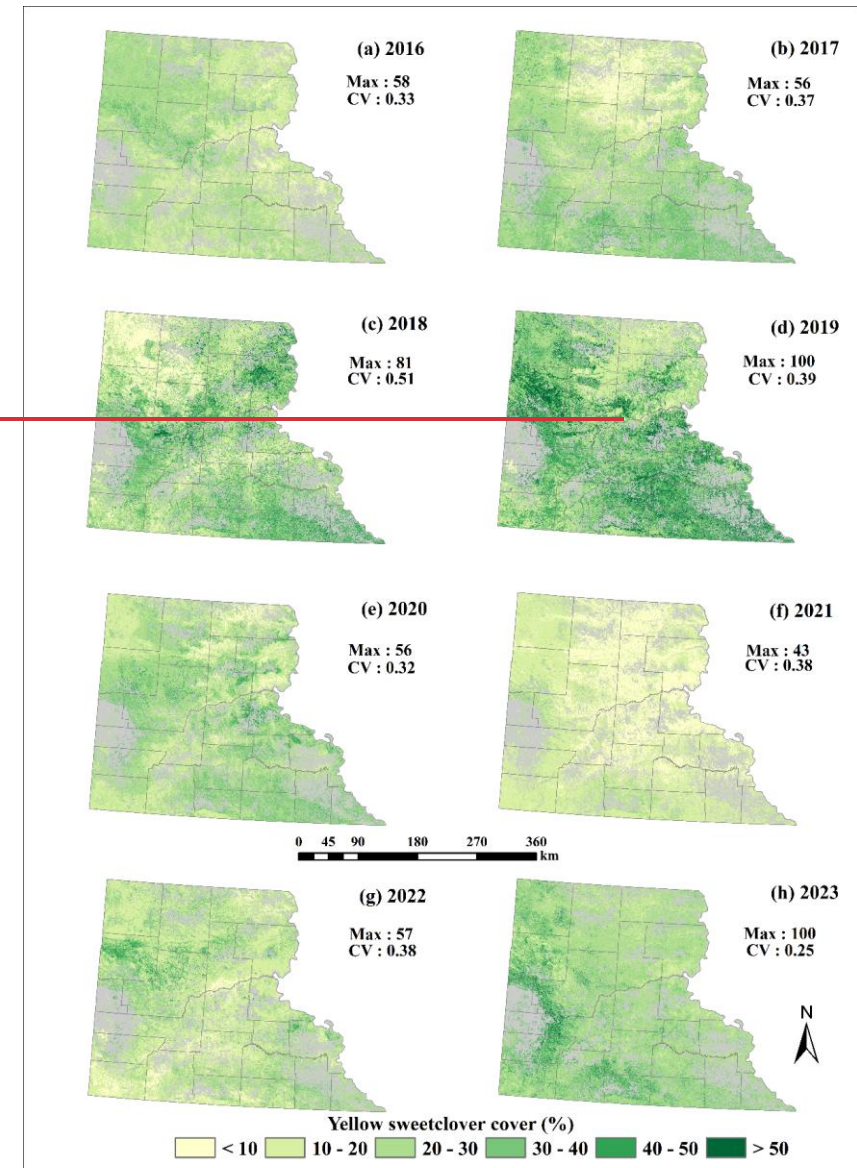
Figure 2 Workflow to predict invasive yellow sweetclover percent cover at 10m resolution using UAS and ancillary data for 2016-2023.



1225



1226
1227 Figure 3 Exemplary Representative figures for three Unmanned Aerial Systems (UAS) sites with
1228 yellow sweetclover (MEOF) blooms (a) UAS orthoimages in green, green and blue band
1229 combination (b) Normalized Difference Yellowness Index (c) Random Forest classified image
1230 showing yellow sweetclover presence and absence (d) yellow sweetclover cover derived at 10m
1231 pixel size.



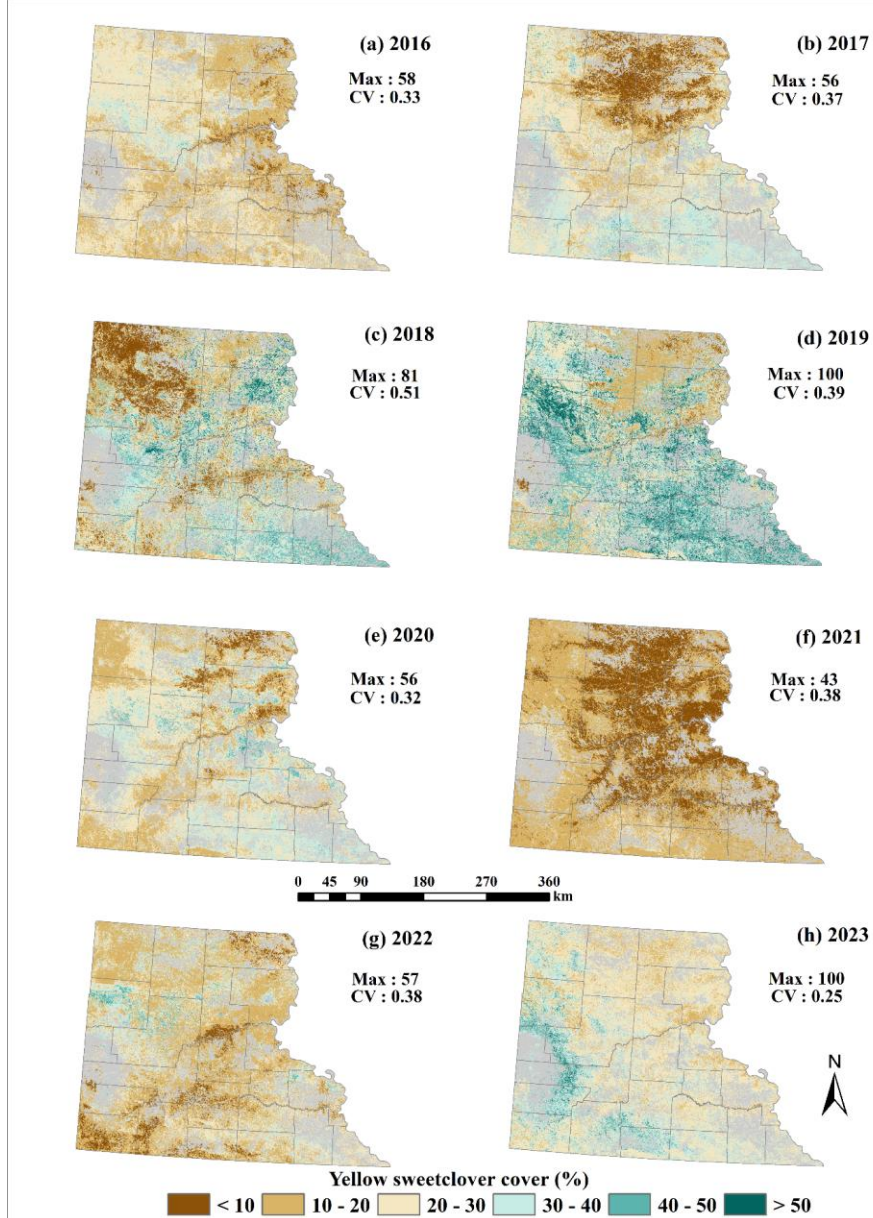
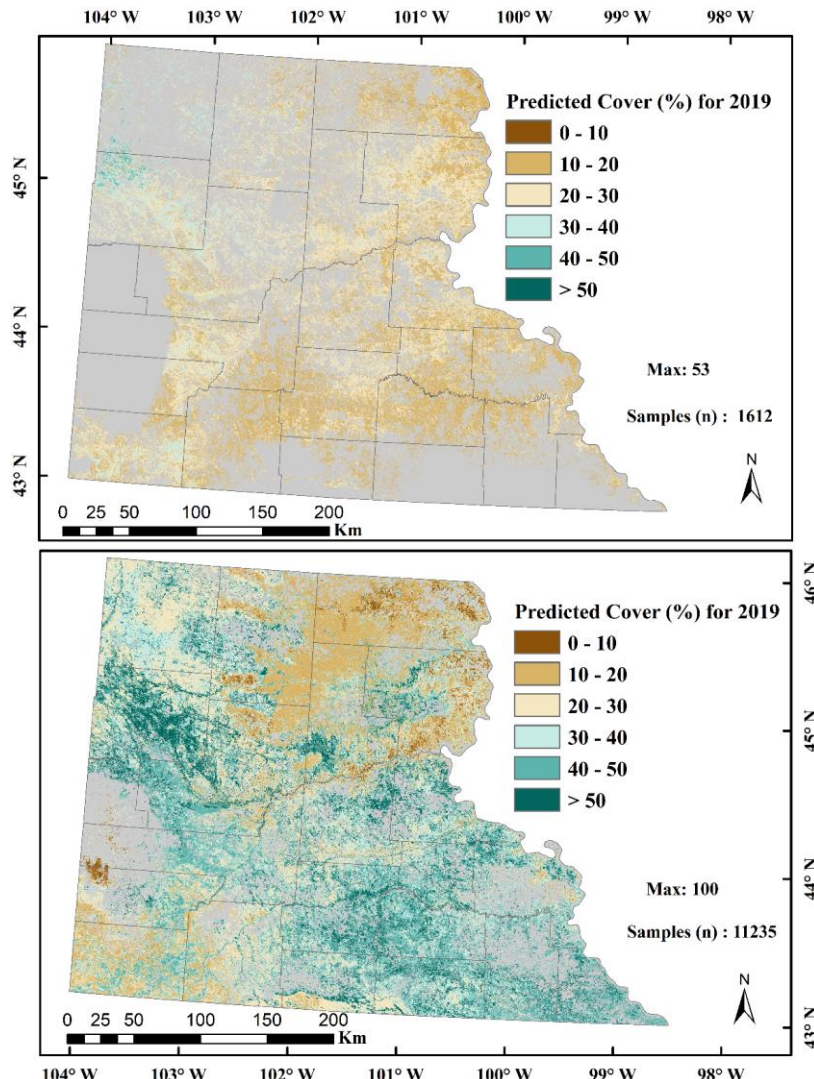


Figure 4 Predicted yellow sweetclover distribution using a generalized Random Forest (RF) regression model for 2016-2023.

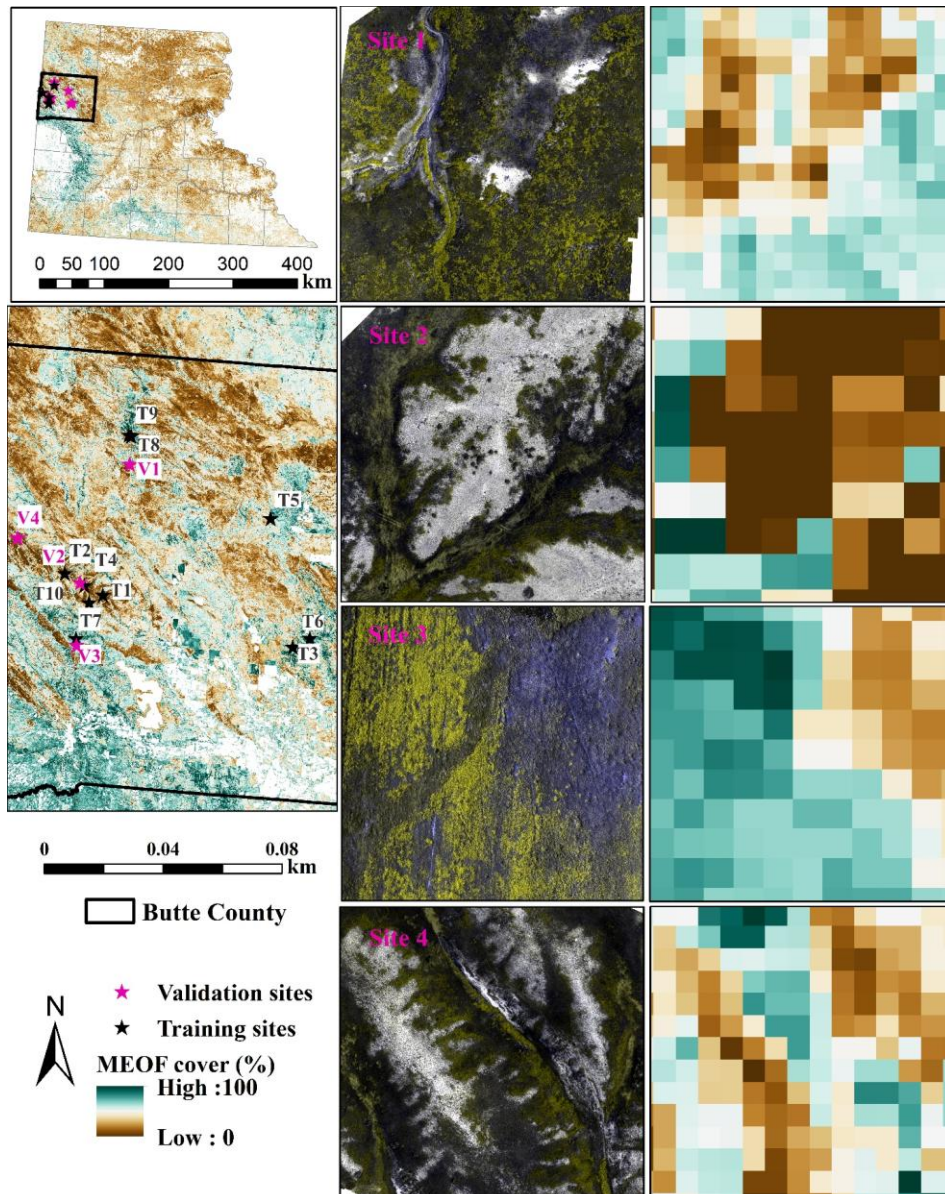
1236



1237

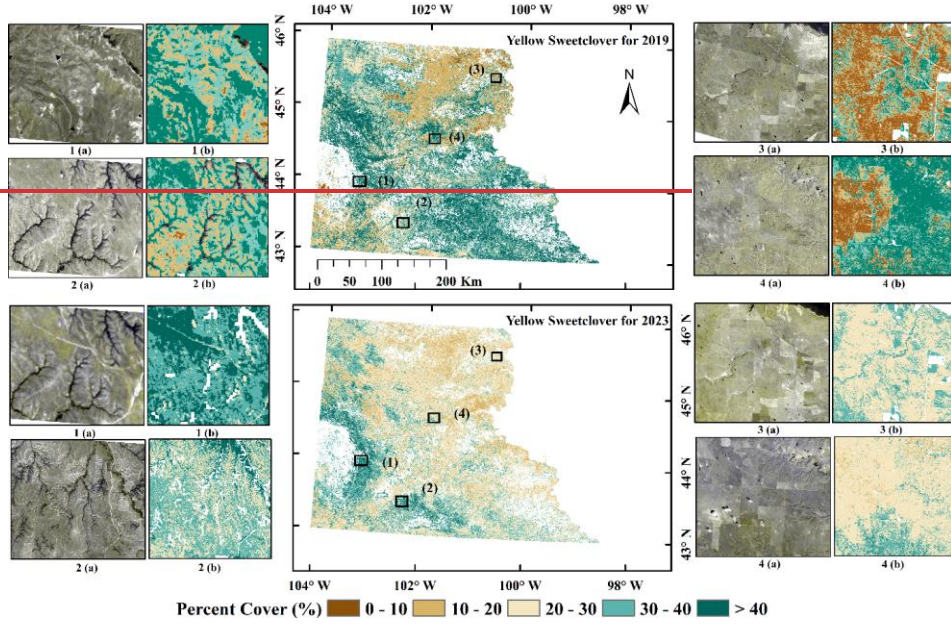
1238 [Figure 5. Comparison of yellow sweetclover \(*Melilotus officinalis*\) cover in western South](#)
 1239 [Dakota rangelands for 2019. \(a\) Percent cover estimates from Saraf et al. \(2023\) based on 1,612](#)
 1240 [samples, showing areas with high probability of yellow sweetclover occurrence. \(b\) Predicted](#)
 1241 [percent cover from the current study using 11,235 samples, highlighting the updated yellow](#)
 1242 [sweetclover cover estimates compared with Saraf et al. \(2023\).](#)

1243 Figure 5 (a) Yellow sweetclover percent cover estimates in the high yellow sweetclover
1244 probability of occurrence regions in the western South Dakota rangelands for 2019 using 1,612
1245 samples (Saraf et al., 2023), (b) Yellow sweet clover predicted for 2019 using 11,235 samples in
1246 the western South Dakota rangelands.

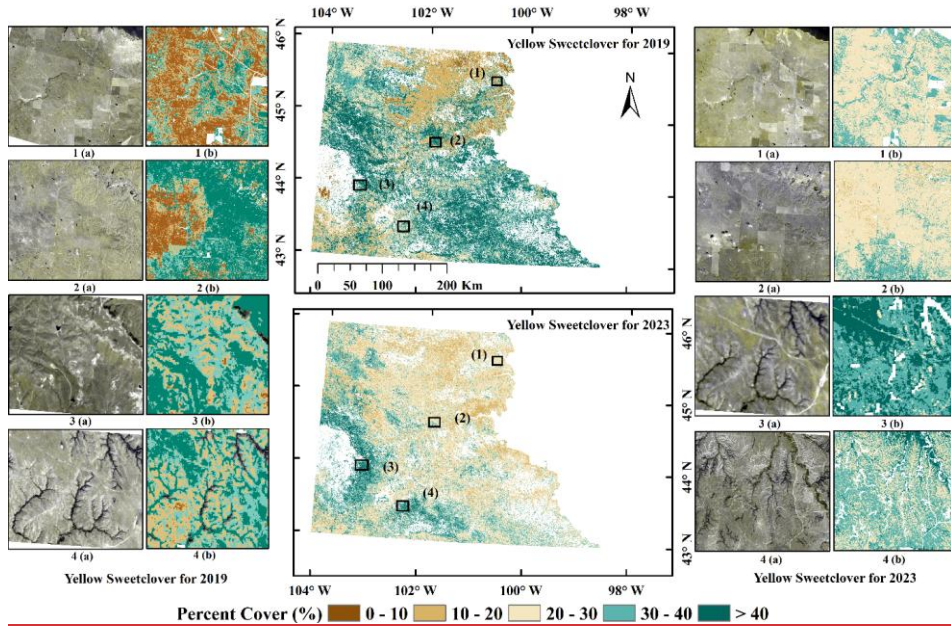


1247

1248 Figure 6. Percent cover estimates for invasive yellow sweetclover for four independent UAS
 1249 validation sites shown in green-green-blue false color combination to highlight yellow
 1250 sweetclover blooms.



Percent Cover (%) 0 - 10 10 - 20 20 - 30 30 - 40 > 40



Percent Cover (%) 0 - 10 10 - 20 20 - 30 30 - 40 > 40

1253 Figure 7. Predicted percent cover estimates for invasive yellow sweetclover (MEOF) at four
1254 different sites represented with numbers for 2019 (left) and 2023 (right). In each site, (a) 3 m
1255 resolution PlanetScope imagery shown in green, green, and blue band combination to highlight
1256 yellow sweetclover blooms, and (b) fractional cover of MEOF. (PlanetScope imagery © Planet
1257 Labs PBC). Predicted percent cover estimates for invasive yellow sweetclover (MEOF) in panel
1258 (a) at four different sites represented with numbers and each site is compared with the
1259 PlanetScope imagery available at 3 m resolution shown in green, green, and blue band
1260 combination to highlight yellow sweetclover blooms in panel (b). (PlanetScope imagery ©
1261 Planet Labs PBC).